Supplement of Atmos. Chem. Phys., 26, 16741–16764, 2026
https://doi.org/10.5194/acp-26-16741-2026-supplement
© Author(s) 2026. CC BY 4.0 License.



Atmospheric Chemistry and Physics
Open Access
EGU

Supplement of

High-frequency monitoring of SO_2 plumes from moderate-scale volcanic eruptions using a synergy of GEO and LEO satellites: a case study of the 2024 Kanlaon eruption

Shangyi Liu et al.

Correspondence to: Zhao-Cheng Zeng (zczeng@pku.edu.cn)

The copyright of individual parts of the supplement might differ from the article licence.

S1. The forward model

In the forward simulations, the top-of-atmosphere radiance received by the sensor is modeled as the summation of four radiative components: (a) surface thermal emission, (b) upwelling atmospheric emission, (c) downwelling atmospheric radiance reflected by the surface, and (d) reflected solar radiation. Molecular and aerosol scattering are considered negligible in the thermal infrared region and are thus excluded. For numerical implementation, the atmosphere is discretized into a fixed 34-layer pressure grid ranging from 1000 hPa to 1 hPa (see Table S1). The vertical resolution is approximately 1 km below 25 km and increases to 2.5 km above this altitude (based on the USSA model). The thickness of the bottom layer is dynamically adjusted based on the actual surface pressure. More detailed description described in Zeng et al. (2023a).

Input parameters for the forward model are derived from multiple high-resolution datasets. Profiles for atmospheric temperature, water vapor, and O_3, along with surface skin temperature and surface pressure, are sourced from the European Centre for Medium-Range Weather Forecasts (ECMWF) Reanalysis v5 (ERA5) (Hersbach et al., 2020). CO_2 profiles are obtained from the ECMWF CAMS model. The prior vertical distribution of SO_2 and other interfering species follow the Line-By-Line Radiative Transfer Model (LBLRTM) standard atmospheric backgrounds. Surface emissivity is derived from the University of Wisconsin-Madison Global Infrared Land Surface Emissivity database (Seemann et al., 2008). To optimize computational efficiency, gas absorption coefficients were pre-calculated using the LBLRTM v12.11 to construct look-up tables (LUTs). This spectroscopic database, based on HITRAN (Clough et al., 2005; Rothman et al., 2013), encompasses 50 pressure levels and 15 temperature levels ranging from 180 K to 320 K at 10 K intervals.

S2. Parameterization and simulations of volcanic ash in the forward model

To investigate the impact of volcanic ash on GIIRS SO_2 retrievals, volcanic ash aerosols are introduced into the forward radiative transfer model to conduct spectral simulation experiments. Fig. S3 illustrates the optical parameterization of volcanic ash and its impact on the simulated spectra. First, Fig. S3(a) shows the real and imaginary parts of the complex refractive index of volcanic ash used in the forward simulations. To calculate the volume extinction of volcanic ash, a lognormal size distribution is adopted in the simulation (the integrated reference number concentration N_0 is set to 3×10^5 cm^{-3}), expressed as:

$$n(r) = \frac{N_0 e^{-\frac{1}{2}\left(\frac{\ln(r)-\ln(r_m)}{\ln(s)}\right)^2}}{\sqrt{2\pi}\ln(s)r} \quad \text{(S1)}$$

where r_m is the median radius and s is the geometric standard deviation. The conversion between the median radius r_m and the effective radius r_{eff} is given by:

$$r_{eff} = r_m e^{(2.5(\ln(s))^2)} \quad \text{(S2)}$$

To evaluate the impact of different particle sizes on the optical properties, multiple sets of effective radii and geometric standard deviations are configured, with their corresponding size distribution curves shown in Fig. S3(b). Based on the aforementioned complex refractive index and size distribution, and assuming volcanic ash particles are volume-equivalent spheres (with a physical density of 2.5 g/cm^3), we calculate the mass extinction coefficient (MEC) and single scattering albedo (SSA) under corresponding parameters using Mie scattering theory, as shown in Fig. S3(c). These calculated results are consistent with the simulated thermal infrared optical properties of volcanic ash presented by Piontek et al. (2021). For the interference analysis of the SO_2 retrieval for the Kanlaon volcanic eruption, the parameter set of r_{eff} = 0.6 μm is selected for the final forward simulations. This selection refers to the measured results of similar volcanic ash samples by Reed et al. (2018) (e.g., the measured r_{eff} = 0.574 μm for the Aso sample). As shown in the right panel of Fig. S3(c), under the selected particle size, the SSA is extremely small (below 0.1) within the GIIRS SO_2 absorption band (1000 to 1131.25 cm^{-1}). This indicates that the extinction of volcanic ash in this band is almost entirely dominated by absorption. Therefore, only the absorption cross-section of volcanic ash is considered in the forward radiative transfer model, ignoring its scattering effect.

Fig. S3(d) details the direct impact on the simulated top-of-atmosphere spectra after introducing volcanic ash at different altitudes in the forward model. In this set of simulations, the altitude of SO_2 is fixed at 10 km with a column amount of 30 DU; the infrared aerosol optical depth (AOD) of volcanic ash is uniformly set to 0.2 at 10 μm, and the ash layers are placed at altitudes of 3 km, 10 km, and 12 km, respectively. The left panel of Fig. S3(d) displays the simulated spectra containing aerosols, and the right panel shows the residuals (Δ radiance) between different spectra. The interference mechanism of volcanic ash can be clearly identified from the residual results: when volcanic ash is located at 3 km (well below the SO_2 plume), the aerosol primarily acts as the underlying thermal radiation background, maintaining a sufficient thermal contrast with the cold SO_2 layer at 10 km. Therefore, the shape of the SO_2 spectral absorption features is preserved, resulting in small spectral residuals. In contrast, when volcanic ash is

located at 10 km (co-located with SO_2) or 12 km (above SO_2), the aerosols strongly absorb the upward radiation from below, producing a significant broadband masking effect. This causes the depth of the observed SO_2 absorption lines to be substantially weakened and the spectral shape features to be altered. Since this retrieval algorithm relies on fitting the SO_2 spectral absorption shape, such signal attenuation caused by co-located or overlying volcanic ash directly leads to severe underestimations in the retrieval results.

To further evaluate the uncertainty introduced by the absorption-only approximation, we compared our FY-GeoAIR model simulations with the Scattering Reference Forward Model (SRFM; Knizek and Grainger, 2026). The SRFM is a line-by-line radiative transfer code that couples the Reference Forward Model (RFM) with the discrete ordinate method (DISORT) an in-house Mie code to rigorously simulate both scattering and absorption of volcanic aerosols. As shown in Fig. S3(e), the simulated top-of-atmosphere radiance spectra from the two models exhibit high consistency across different ash layer altitudes. Although minor spectral residuals (FY − SRFM) arise from the redistribution of upwelling thermal radiation by multiple scattering, these deviations remain a secondary effect compared to the massive broadband masking caused by ash absorption. The overall SO_2 absorption shape and line depths are well preserved in the FY-GeoAIR model.

Reference

Clough, S. A., Shephard, M. W., Mlawer, E. J., Delamere, J. S., Iacono, M. J., Cady-Pereira, K., Boukabara, S., & Brown, P. D. (2005). Atmospheric radiative transfer modeling: A summary of the AER codes. Journal of Quantitative Spectroscopy and Radiative Transfer, 91(2), 233–244. https://doi.org/10.1016/j.jqsrt.2004.05.058

Hersbach, H., Bell, B., Berrisford, P., Hirahara, S., Horányi, A., Muñoz-Sabater, J., Nicolas, J., Peubey, C., Radu, R., Schepers, D., Simmons, A., Soci, C., Abdalla, S., Abellan, X., Balsamo, G., Bechtold, P., Biavati, G., Bidlot, J., Bonavita, M., … Thépaut, J. (2020). The ERA5 global reanalysis. Quarterly Journal of the Royal Meteorological Society, 146(730), 1999–2049. https://doi.org/10.1002/qj.3803

Knizek, A., & Grainger, R. G. (2026). Scattering Reference Forward Model (Version 1.5.1) [Software]. PyPI. https://pypi.org/project/SRFM/

Piontek, D., Hornby, A. J., Voigt, C., Bugliaro, L., & Gasteiger, J. (2021). Determination of complex refractive indices and optical properties of volcanic ashes in the thermal infrared based on generic petrological compositions. Journal of Volcanology and Geothermal Research, 411, 107174. https://doi.org/10.1016/j.jvolgeores.2021.107174

Reed, B. E., Peters, D. M., McPheat, R., & Grainger, R. G. (2018). The complex refractive index of volcanic ash aerosol retrieved from spectral mass extinction. Journal of Geophysical Research: Atmospheres, 123, 1339–1350. https://doi.org/10.1002/2017JD027362

Rothman, L. S., Gordon, I. E., Babikov, Y., Barbe, A., Chris Benner, D., Bernath, P. F., Birk, M., Bizzocchi, L., Boudon, V., Brown, L. R., Campargue, A., Chance, K., Cohen, E. A., Coudert, L. H., Devi, V. M., Drouin, B. J., Fayt, A., Flaud, J.-M., Gamache, R. R., … Wagner, G. (2013). The HITRAN2012 molecular spectroscopic database. Journal of Quantitative Spectroscopy and Radiative Transfer, 130, 4–50. https://doi.org/10.1016/j.jqsrt.2013.07.002

Seemann, S. W., Borbas, E. E., Knuteson, R. O., Stephenson, G. R., & Huang, H.-L. (2008). Development of a global infrared land surface emissivity database for application to clear sky sounding retrievals from multispectral satellite radiance measurements. Journal of Applied Meteorology and Climatology, 47(1), 108–123. https://doi.org/10.1175/2007JAMC1590.1

Zeng, Z.-C., Lee, L., & Qi, C. (2023a). Diurnal carbon monoxide observed from a geostationary infrared hyperspectral sounder: First result from GIIRS on board FengYun-4B. Atmospheric Measurement Techniques, 16(12), 3059–3083. https://doi.org/10.5194/amt-16-3059-2023

Table S1. Pressure-level definitions in our forward model vertical grid

Layer idex	Top Pressure (hPa)	Layer idex	Top Pressure
1	1013	19	75.65
2	898.8	20	64.67
3	795.0	21	55.29
4	701.2	22	47.29
5	616.6	23	40.47
6	540.5	24	34.67
7	472.2	25	29.72
8	411.1	26	25.49
9	356.5	27	17.43
10	308.0	28	11.97
11	265.0	29	8.01
12	227.0	30	5.75
13	194.0	31	4.15
14	165.8	32	2.87
15	141.7	33	2.06
16	121.1	34	1.49
17	103.5	35	1.09
18	88.5		

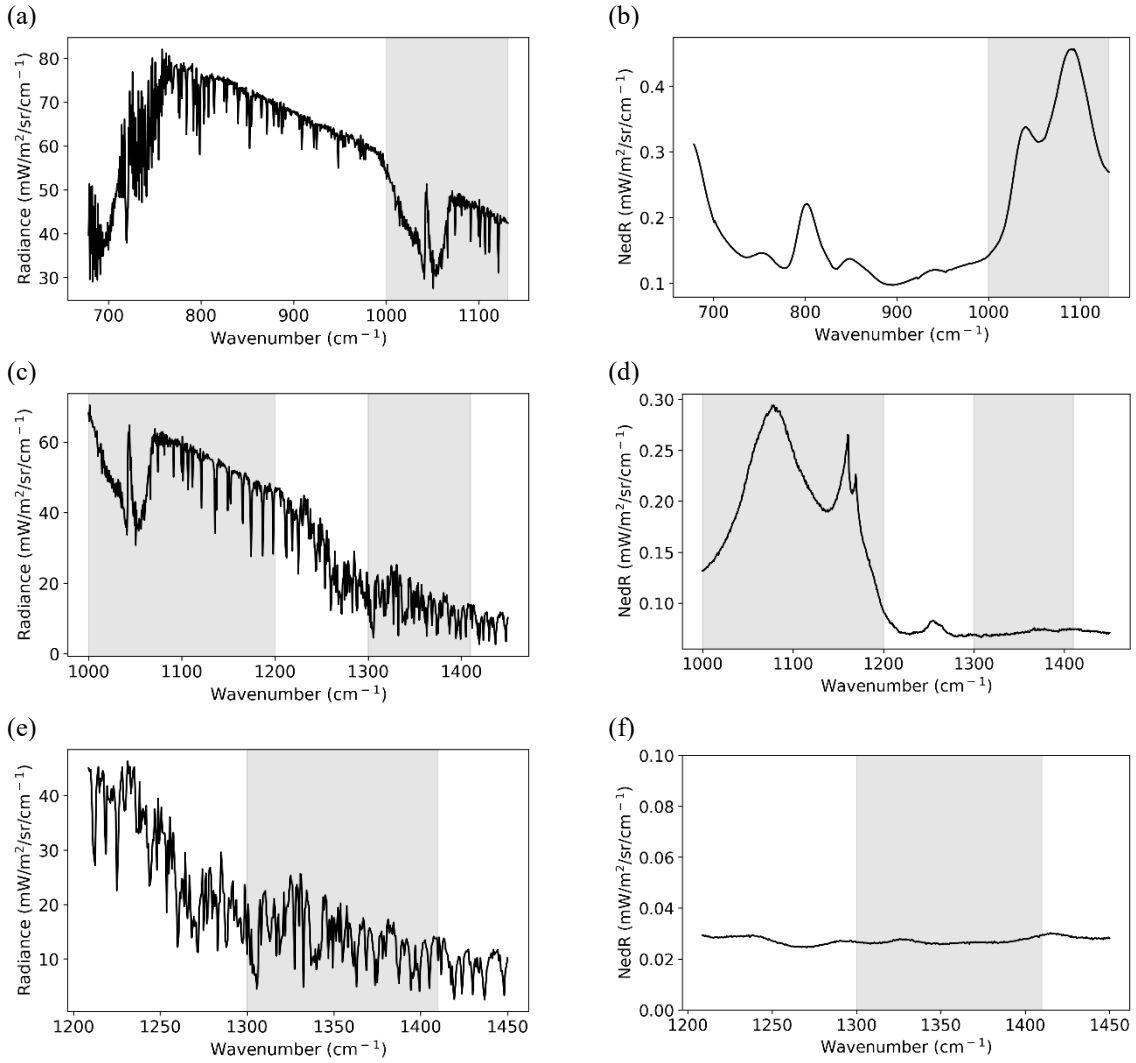

Figure S1. Spectral characteristics and noise performance of the hyperspectral infrared sounders used in this study. (a, c, e) Mean observed long-wave infrared spectra from FY-4B/GIIRS, FY-3E/3F HIRAS, and JPSS-1/2 CrIS, respectively, collected on June 2, 2024, over the potential volcanic plume region. (b, d, f) Corresponding on-orbit Noise Equivalent differential Radiance (NEdR) for each sensor. The gray shaded regions indicate the spectral windows selected for the physical retrieval algorithm: $\nu 1$ (1000–1200 cm^{-1}) and $\nu 3$ (1300–1410 cm^{-1}).

(a)

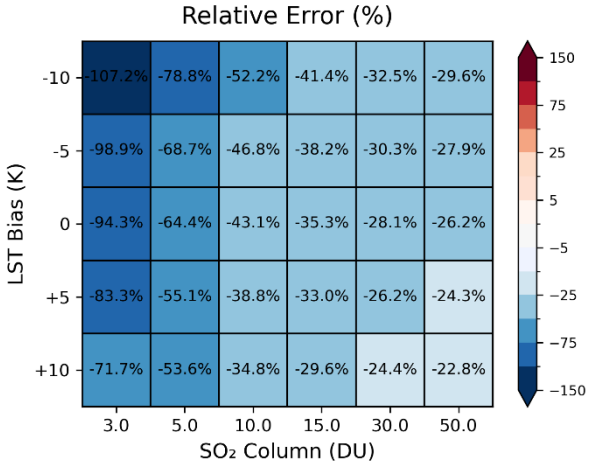

(b)

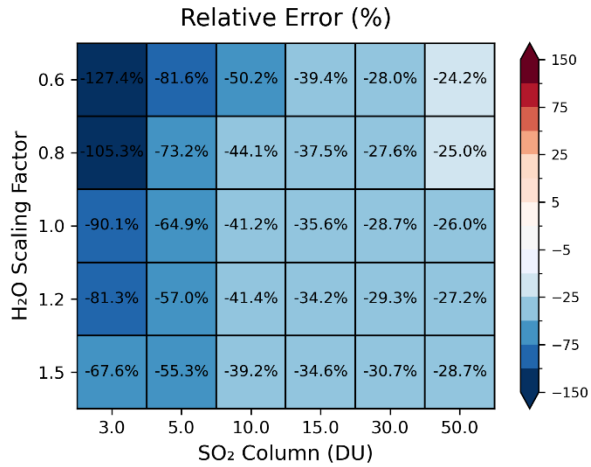

(c)

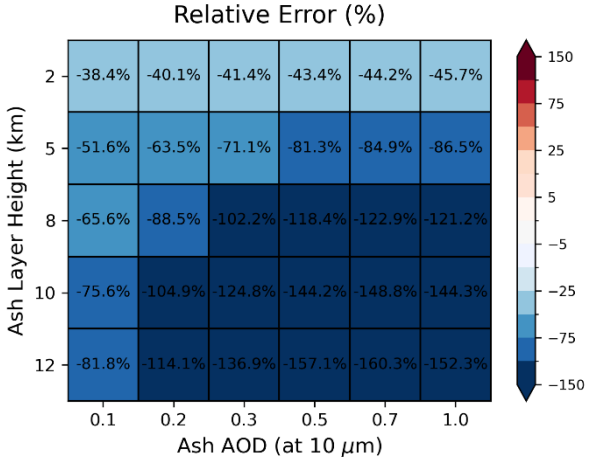

Figure S2. Sensitivity analysis of the of FY-4B/GIIRS SO_2 retrievals under simulated environmental perturbations. Heatmaps show the retrieval relative errors induced by (a) surface temperature variations (-10 K to +10 K), (b) scaled water vapor profiles (0.6 to 1.5), and (c) volcanic ash layer height (2 to 12 km) as a function of infrared ash aerosol optical depth (AOD) at 10 μm for a fixed SO_2 plume (30 DU at 10 km altitude).

(a) (b)

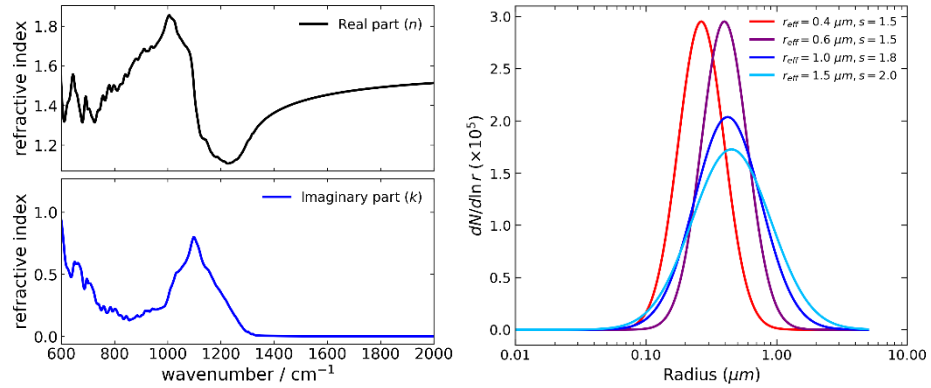

(c)

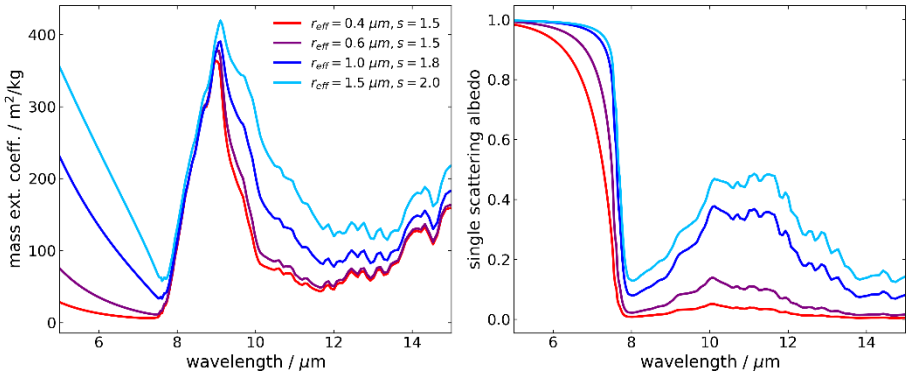

(d)

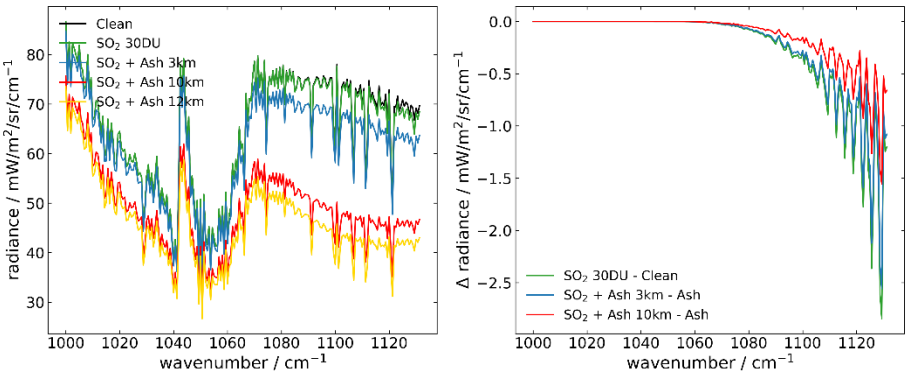

(e)

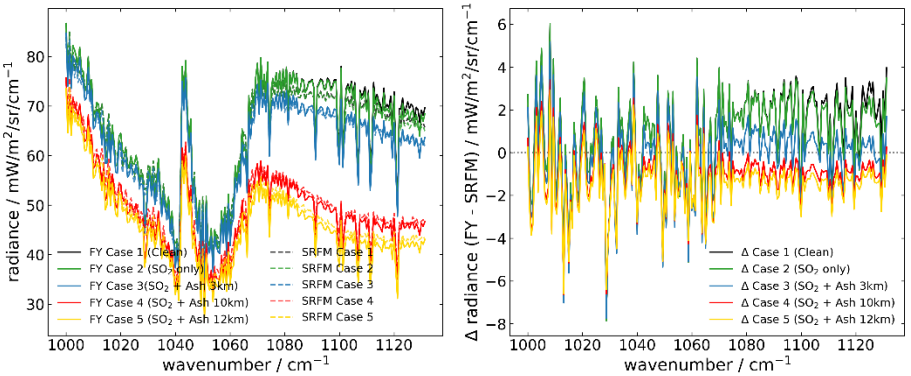

Figure S3. (a) Real and imaginary parts of the complex refractive index of volcanic ash used in the simulations. (b) Lognormal particle size distribution curves configured with different effective radii and geometric standard deviations. (c) Mass extinction coefficient and single scattering albedo calculated using Mie scattering theory. (d) Simulated top-of-atmosphere spectra (left) and the spectral residuals (right) after introducing volcanic ash (AOD = 0.2 at 10 μm) at different altitudes in the forward model. The SO_2 layer is fixed at 10 km with a column amount of 30 DU in all simulations. (e) Comparison of the simulated top-of-atmosphere radiance spectra between the FY-

GeoAIR model (solid lines) and the SRFM model (dashed lines) across different atmospheric cases (left), and their corresponding spectral radiance differences (FY − SRFM) (right).

145

(a)

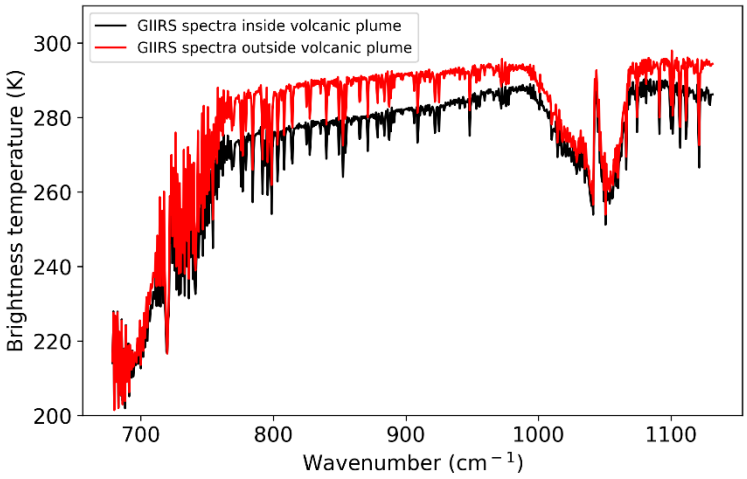

(b)

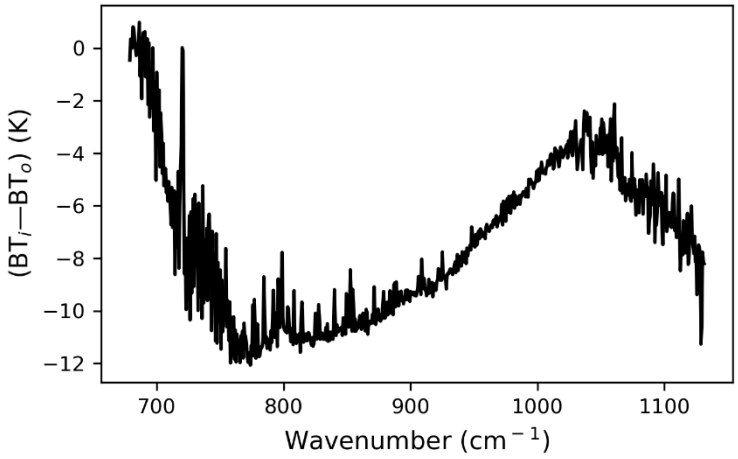

146 Figure S4. (a) FY-4B/GIIRS LWIR spectra (in brightness temperature (BT)) recorded on 3 June 2024 (16.3 UTC).
147 The black curve denotes the spectrum measured within the volcanic plume, and the spectrum in red is taken from
148 a nearby pixel outside the plume. (b) The BT difference ((ΔBT = BT_in − BT_out) between the two spectra,
149 showing the spectral signatures of ice crystal, volcanic ash and SO_2 in the ν1 band.
150

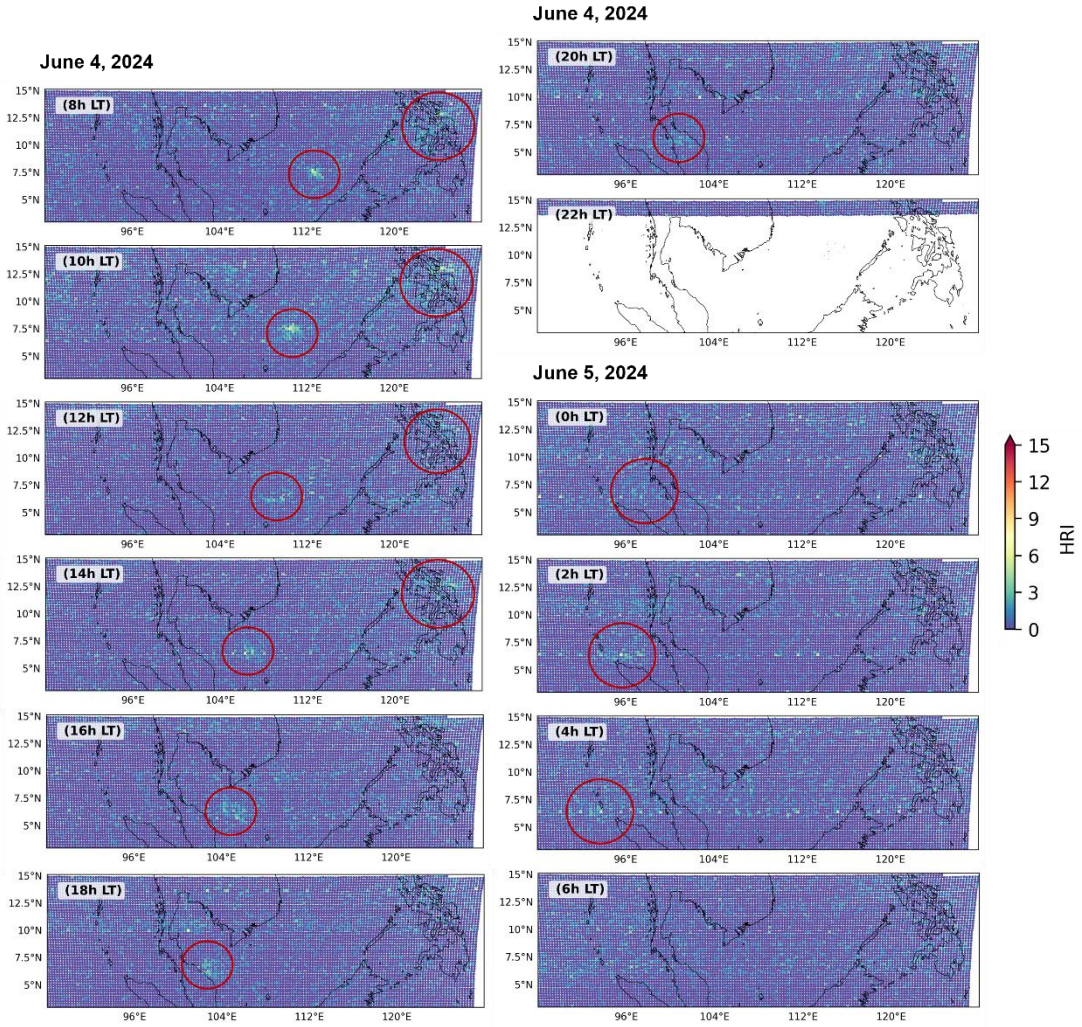

Figure S5. Spatial distribution of the SO_2 HRI derived from FY-4B/GIIRS observations subsequent to the period shown in Figure 5. The panels cover the remaining observation hours on June 4 and 0h–6h LT on June 5, 2024. Red circles indicate areas with high HRI values, tracking the core of the volcanic plume.

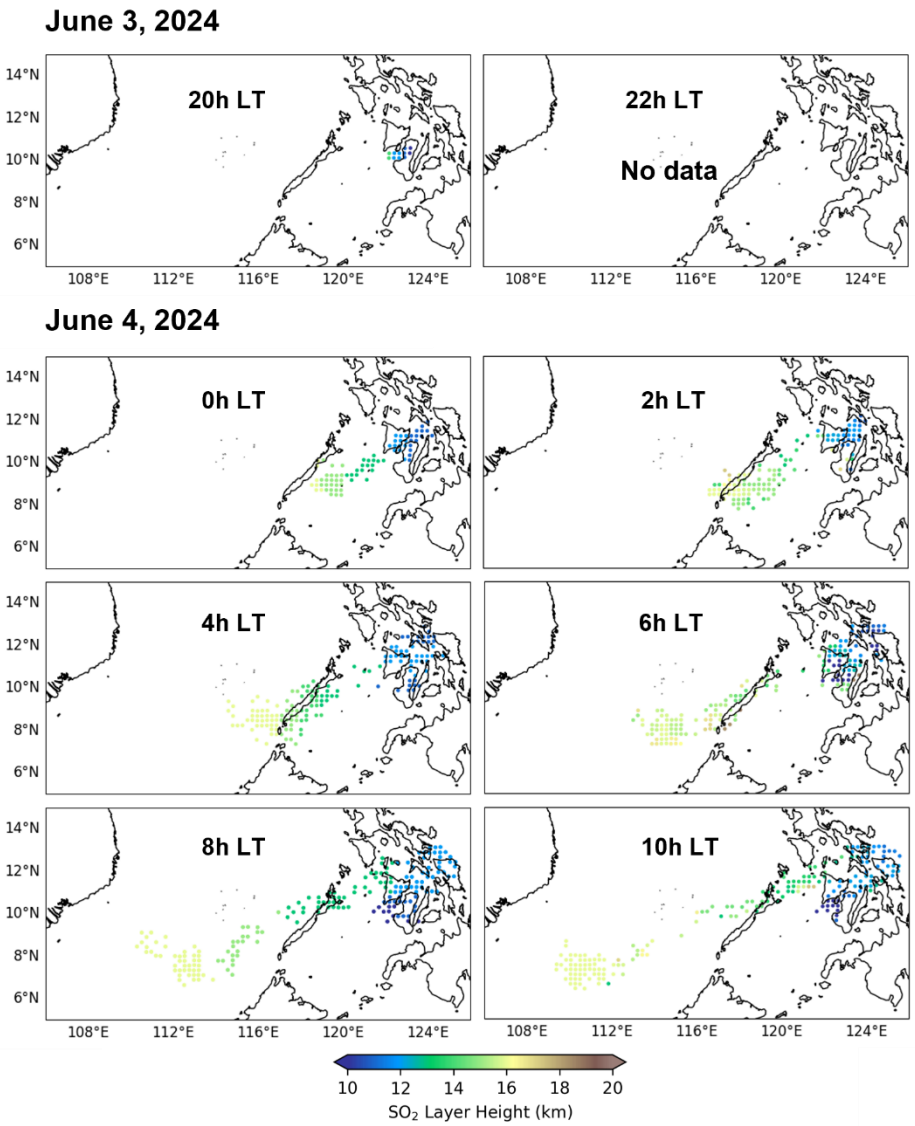

Figure S6. Spatial distribution of the SO_2 plume layer height for FY-4B/GIIRS SO_2 total column retrievals. The plume height information is derived from synergistic observations by FY-3E/F HIRAS and JPSS-1/2 CrIS.

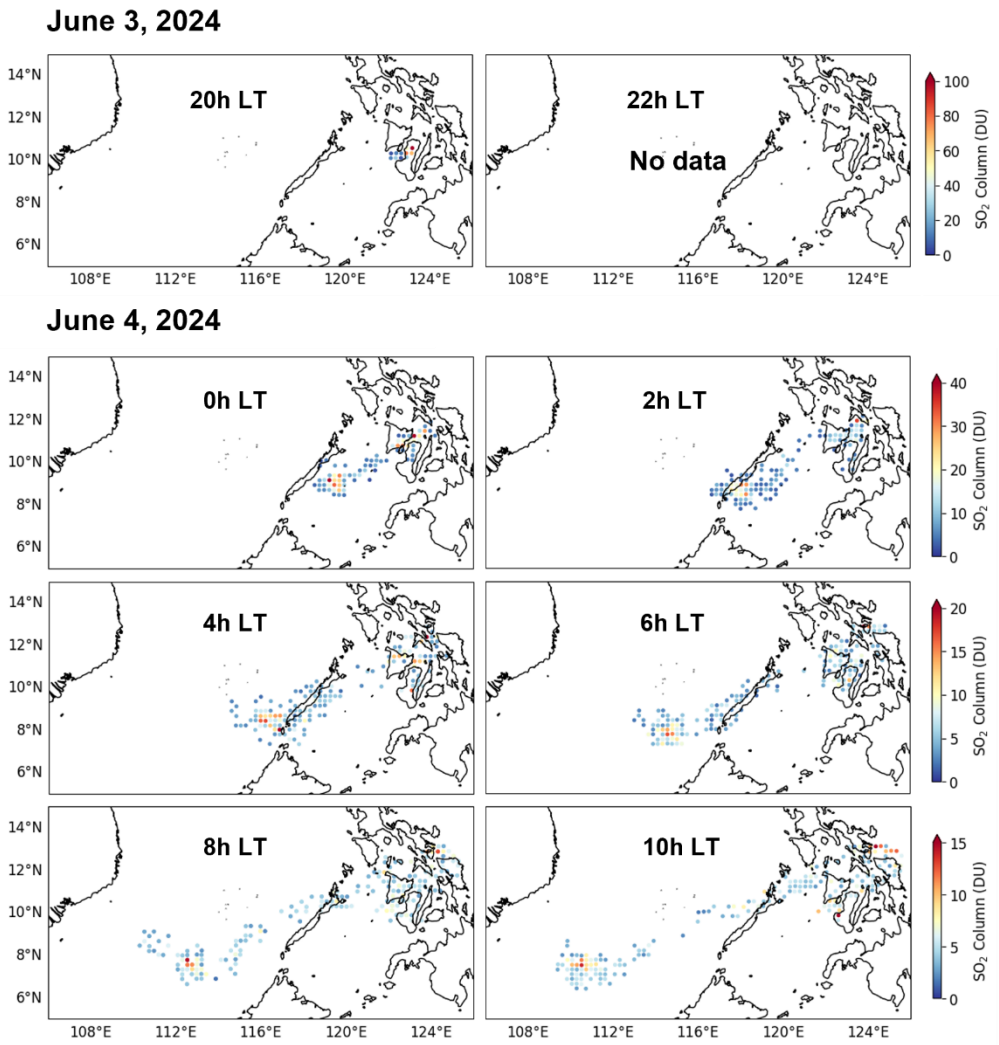

Figure S7. Spatial distribution of SO_2 total column retrieved from FY-4B/GIIRS. The panels correspond to the observations shown in Fig. 5 but within independent color scales.

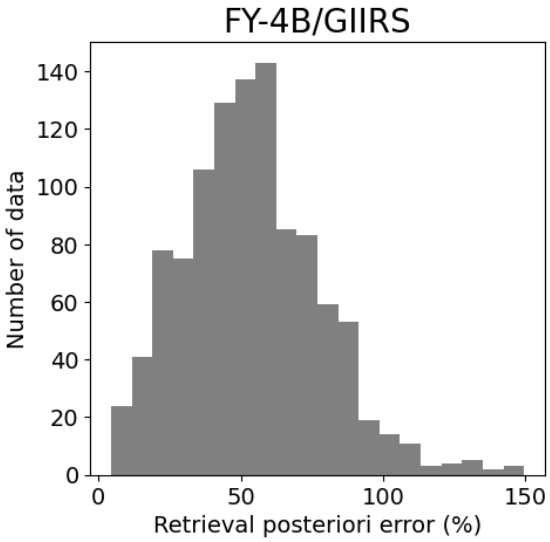

Figure S8. Estimated posterior retrieval error for FY-4B/GIIRS SO_2 total column. The histogram illustrates the statistical spread of retrieval uncertainties, with a mean estimated error of 53.7 ± 24.1%.

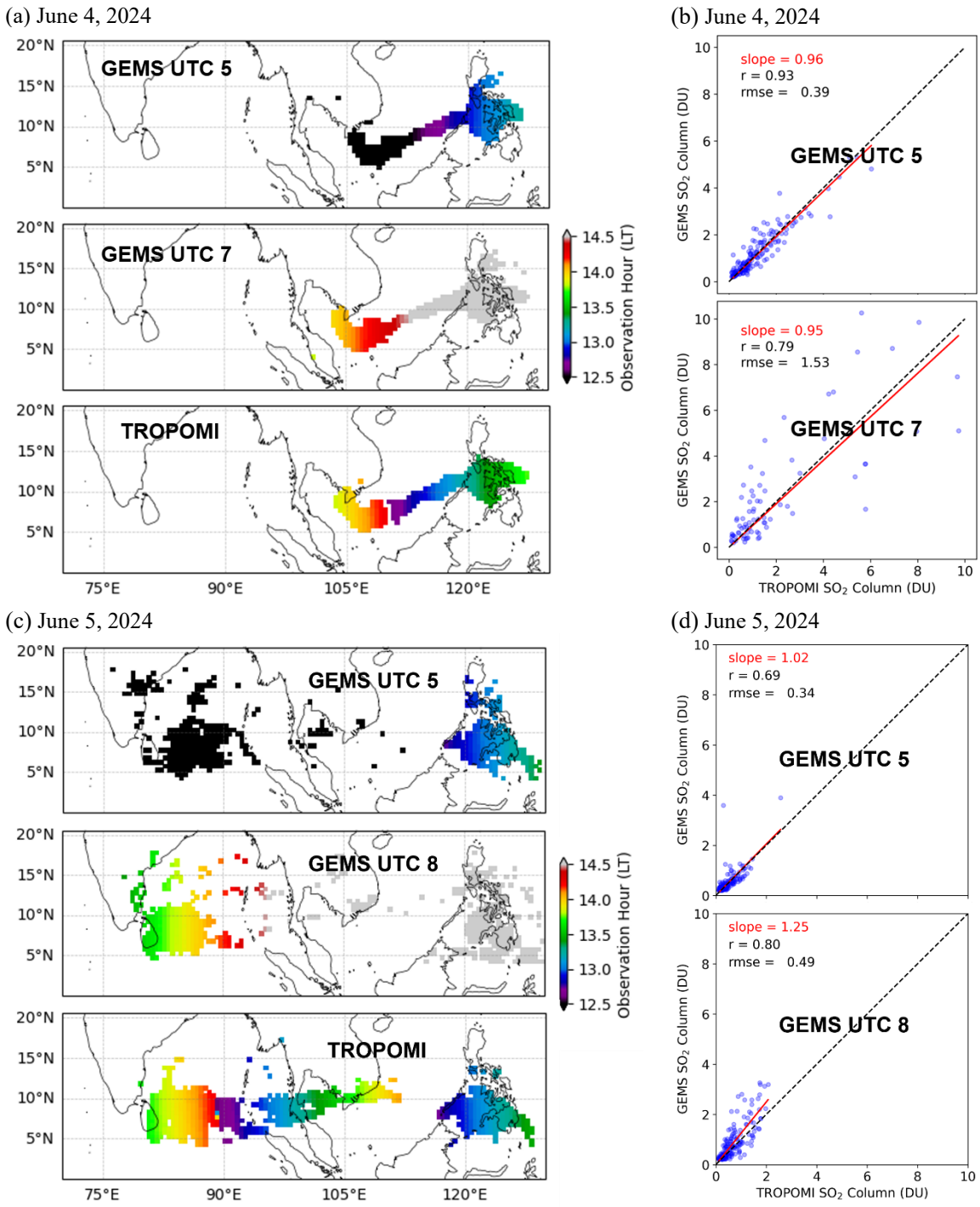

Figure S9. Bias correction of GEMS SO_2 results based on TROPOMI benchmarks. (a, c) Spatial distribution and observation times of the SO_2 pixels used for spatiotemporal matching on (a) June 4 and (c) June 5. (b, d) Scatter plots comparing the bias-corrected GEMS SO_2 total column (scaled by a factor of 0.5) with coincident TROPOMI observations for (b) June 4 and (d) June 5.

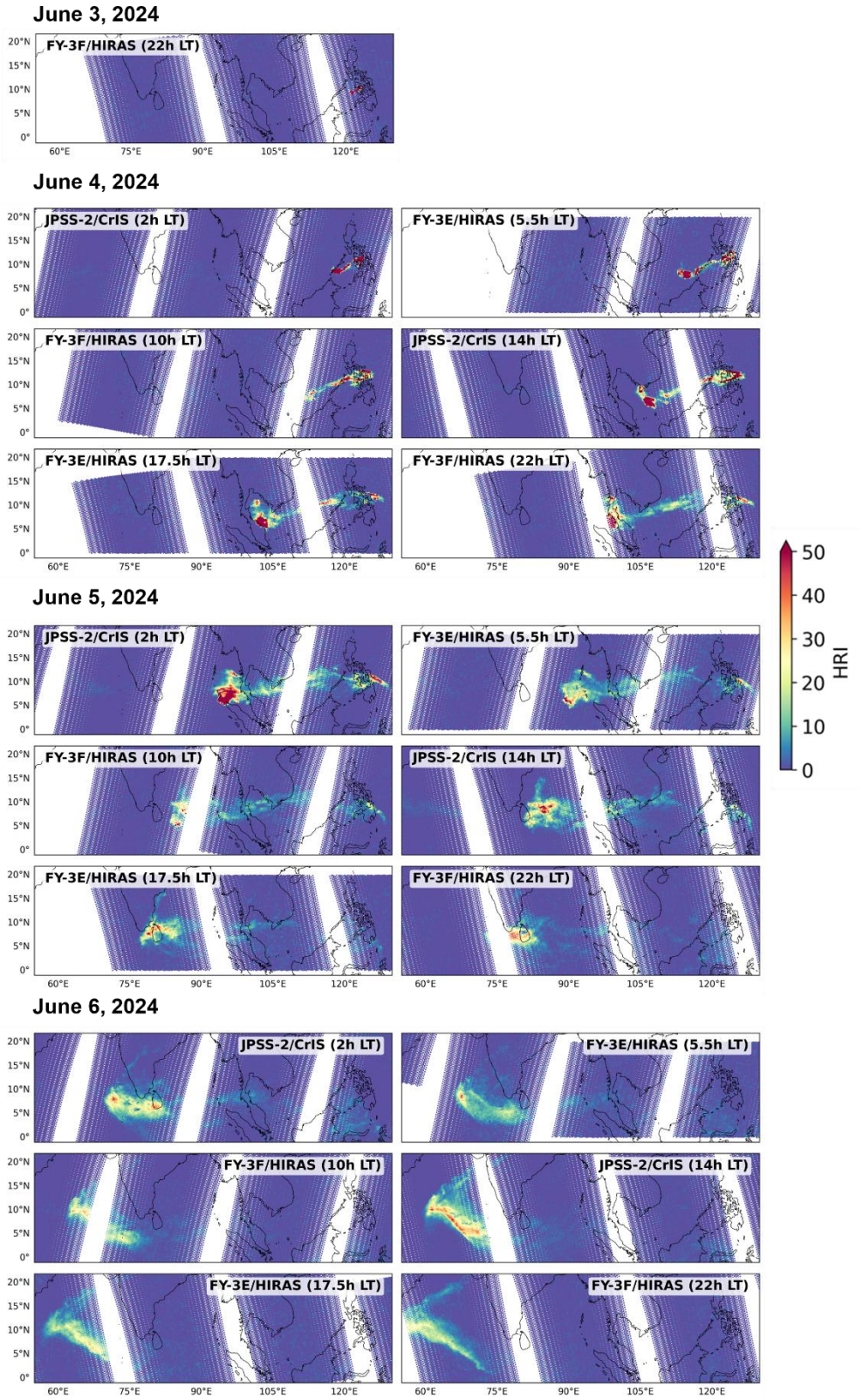

Figure S10. Spatial distribution of the SO_2 HRI derived from FY-3E/F HIRAS and JPSS-2 CrIS during June 3–6, 2024.

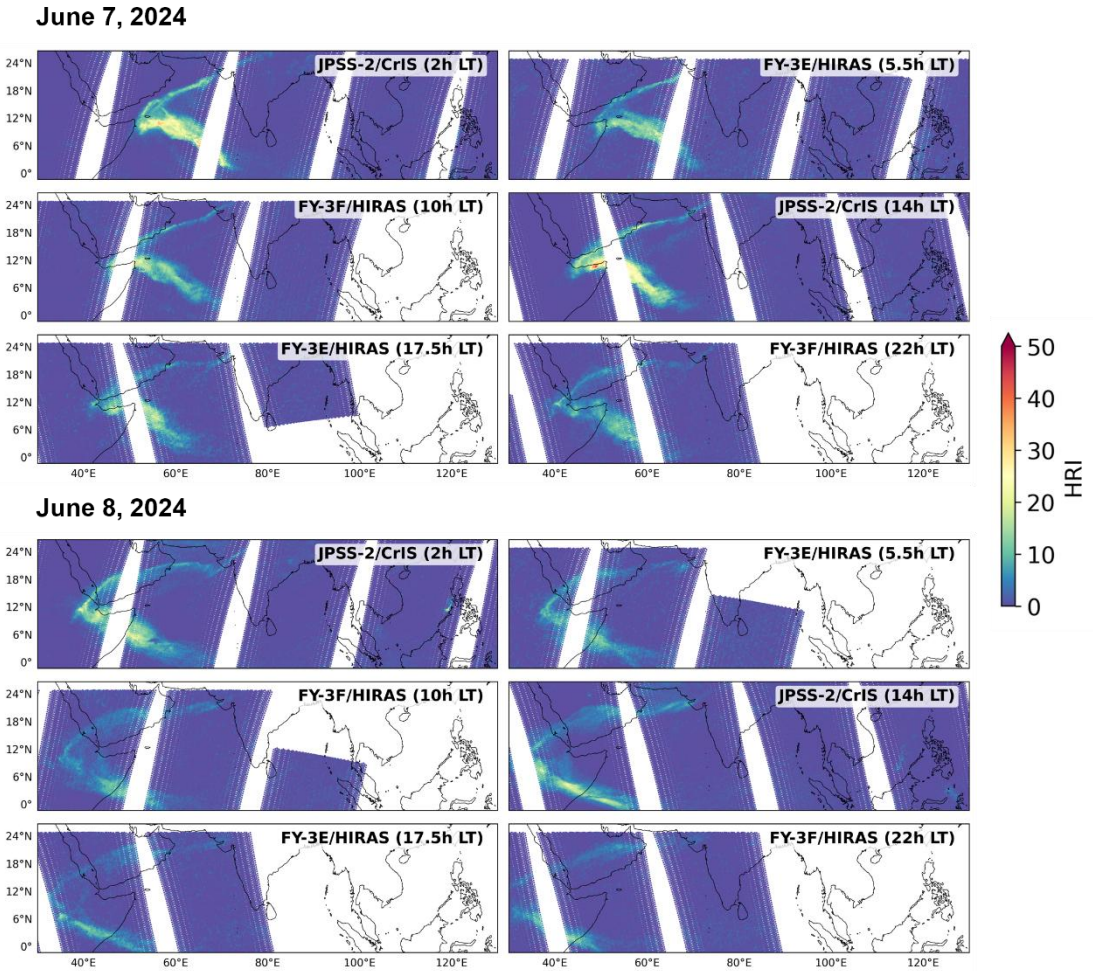

Figure S11. Same as Fig. S10, but for June 7 and 8, 2024.

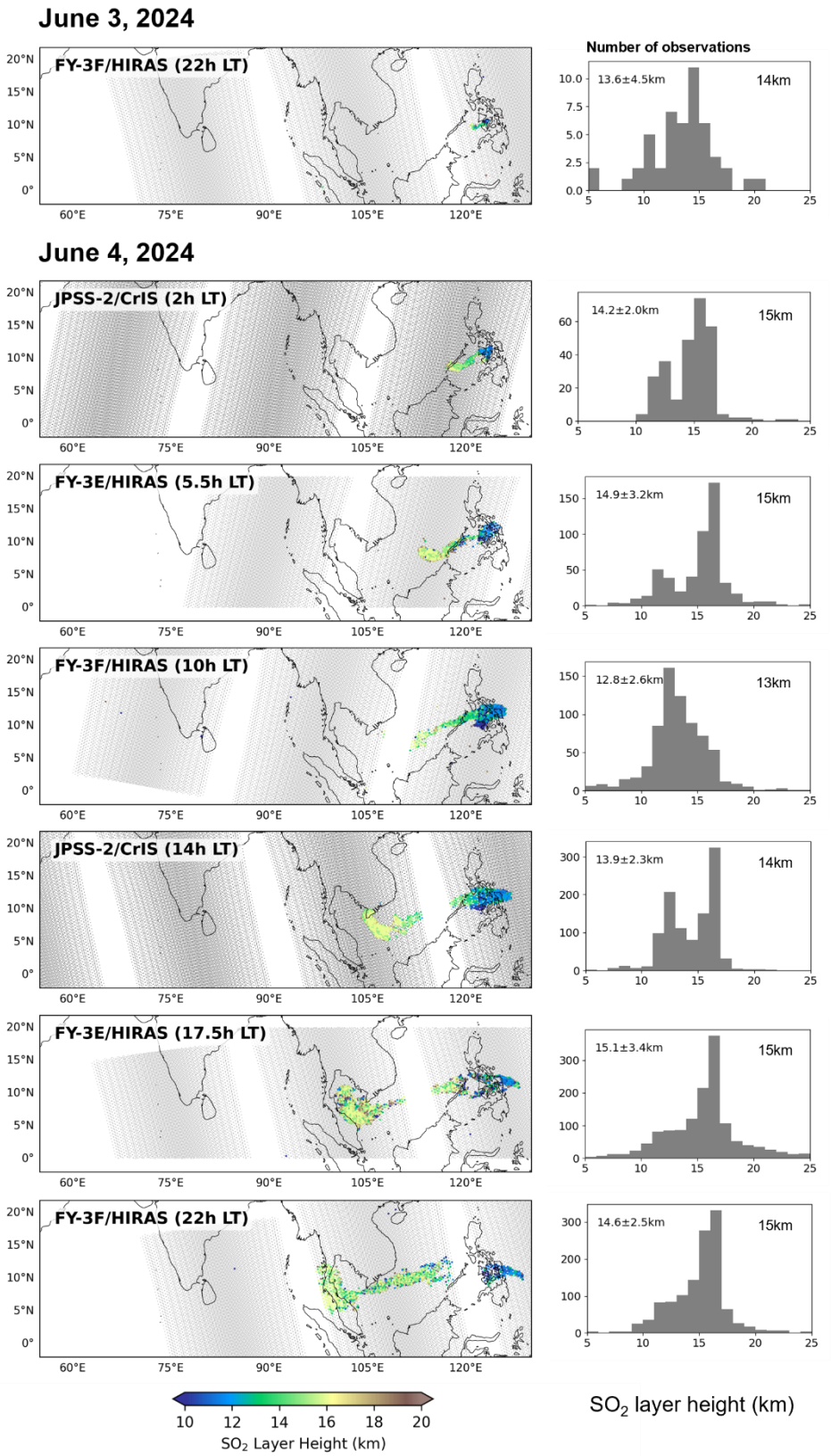

Figure S12. The spatial distribution of the estimated SO_2 layer height and the corresponding histograms for the observations on June 3 and 4, 2024. The inset numbers within each histogram indicate the statistical characteristics of SO_2 height: the values on the left represent the mean ± standard deviation, while the value on the right represents the median.

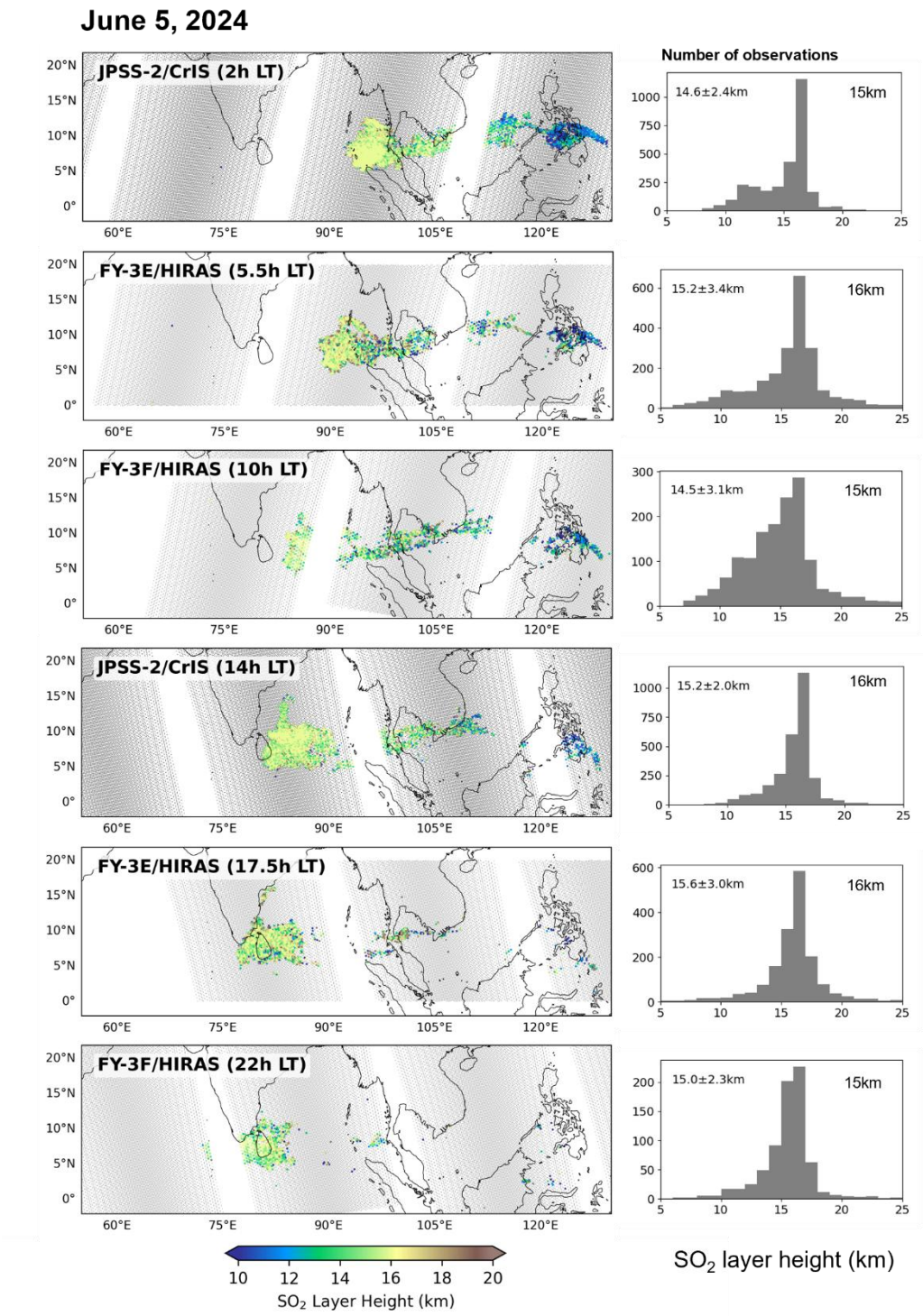

Figure S13. Same as Fig. S12, but for June 5, 2024.

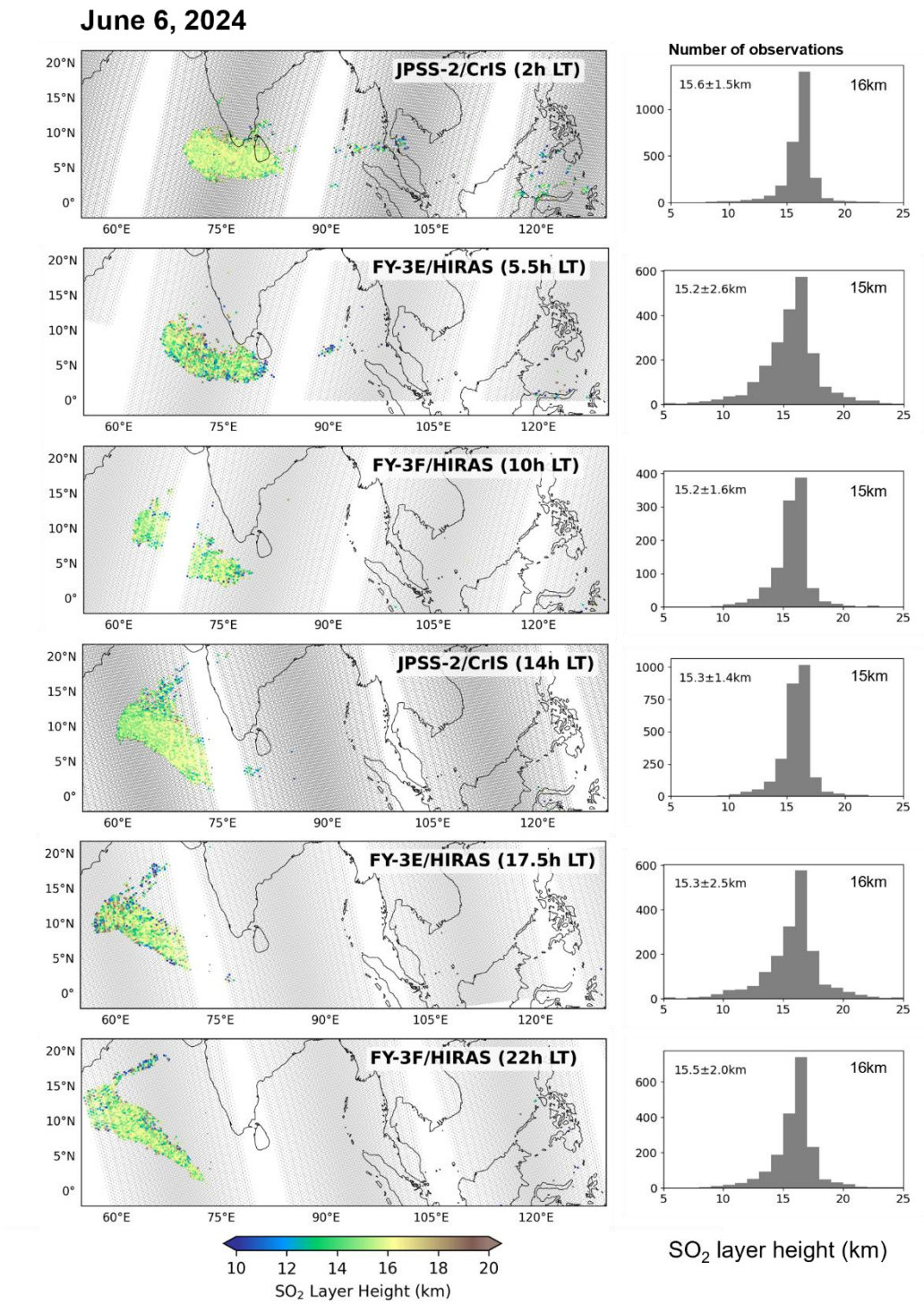

Figure S14. Same as Fig. S12, but for June 6, 2024.

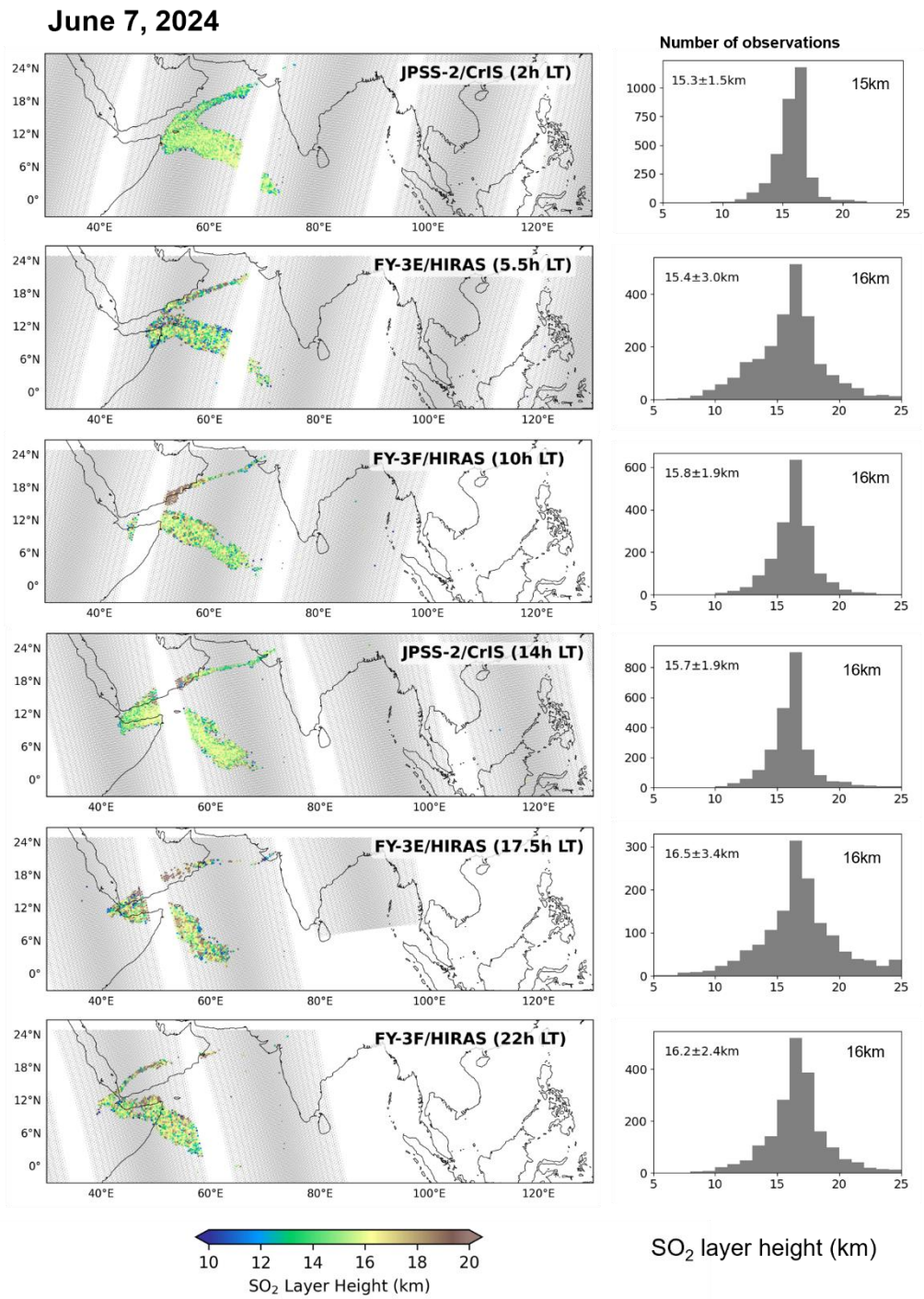

Figure S15. Same as Fig. S12, but for June 7, 2024.

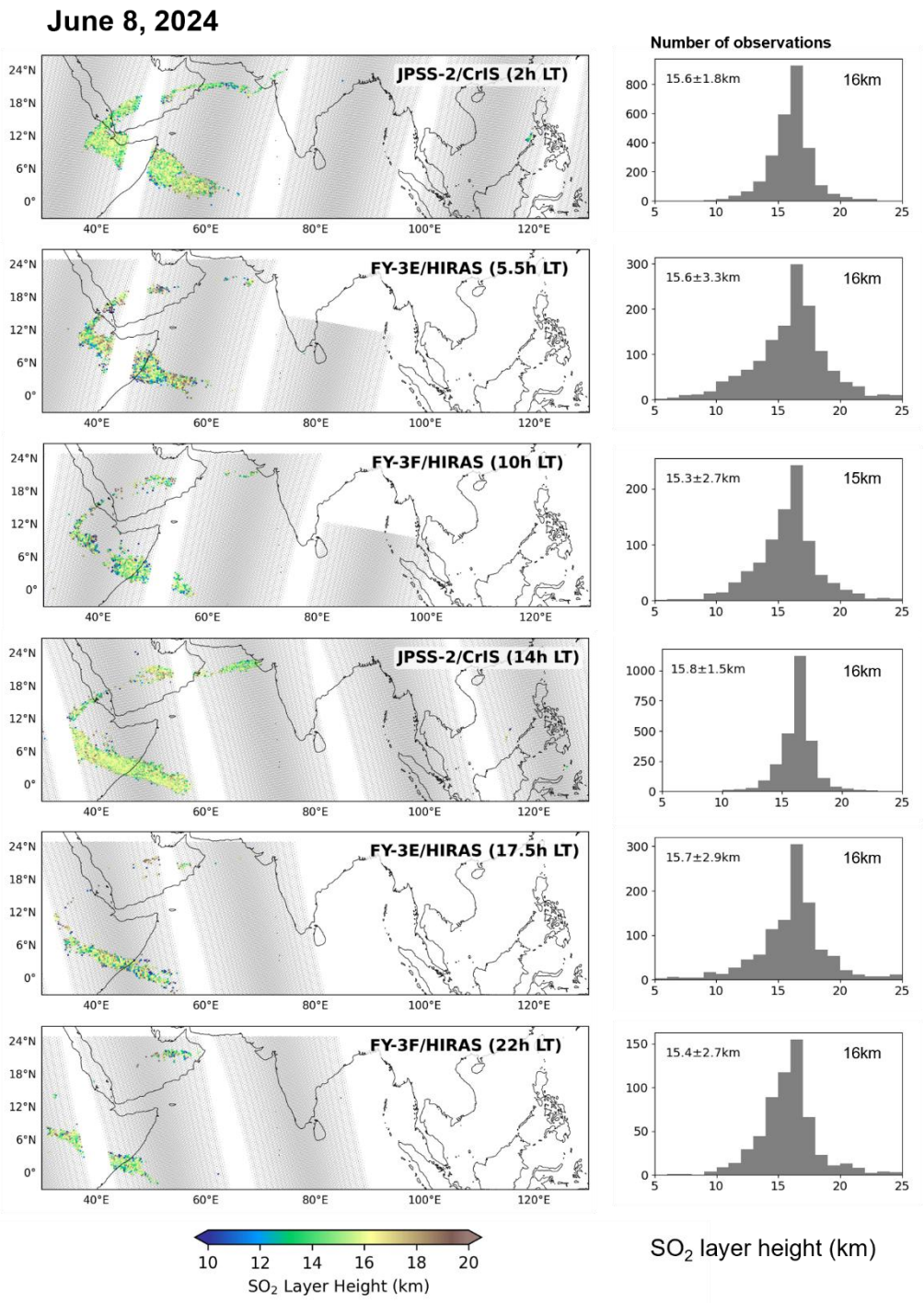

Figure S16. Same as Fig. S12, but for June 8, 2024.

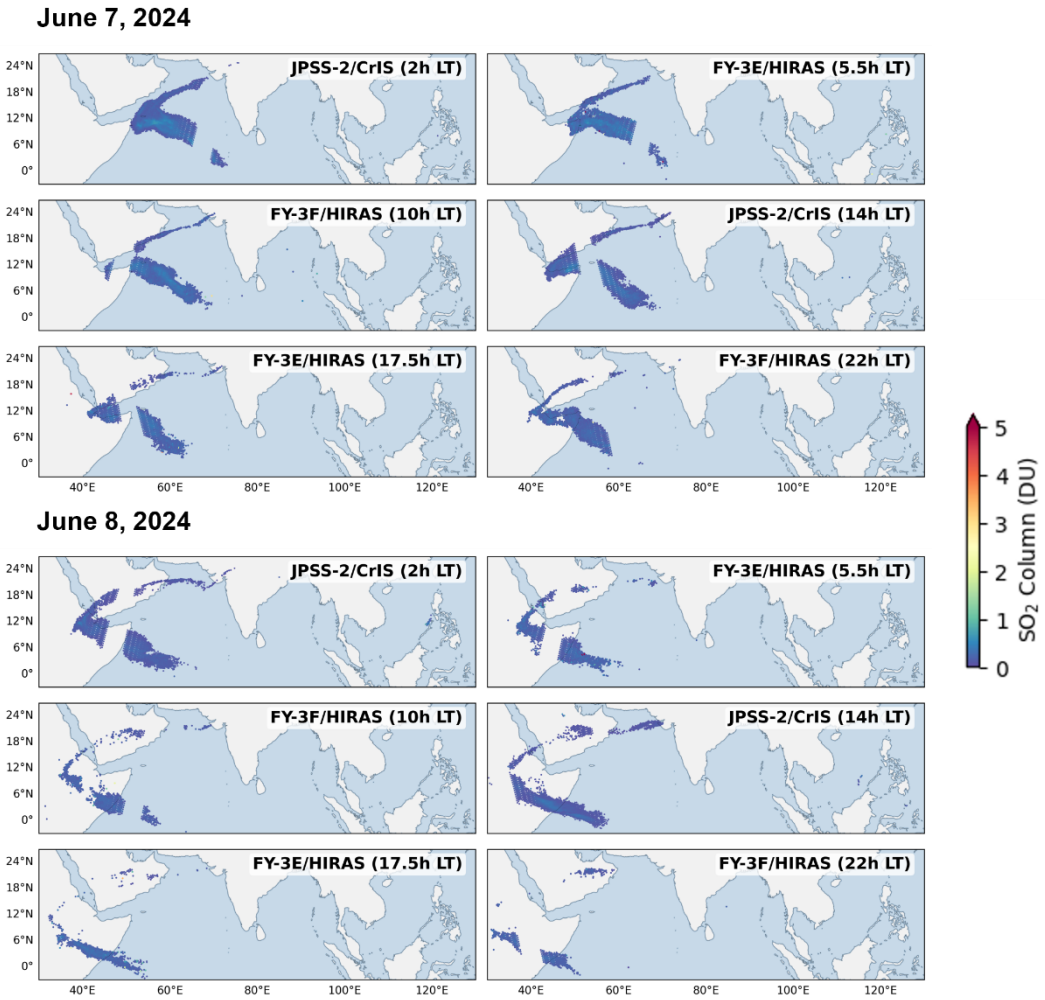

Figure S17. Same as Fig. 7, but for June 7 and 8, 2024.

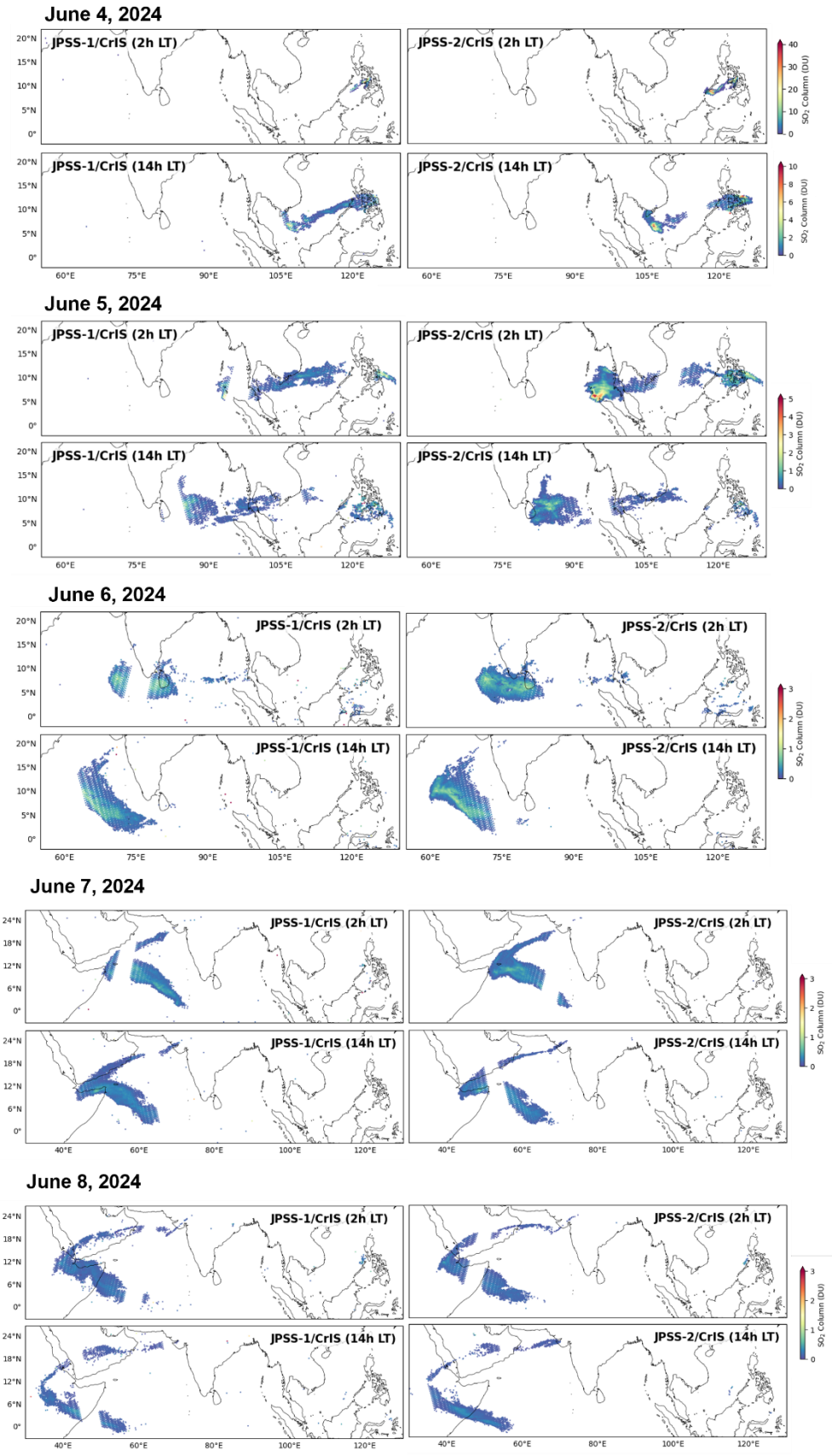

Figure S18. Spatiotemporal evolution of volcanic SO_2 total columns retrieved from JPSS-1/2 CrIS observations during June 4–8, 2024.

(a)

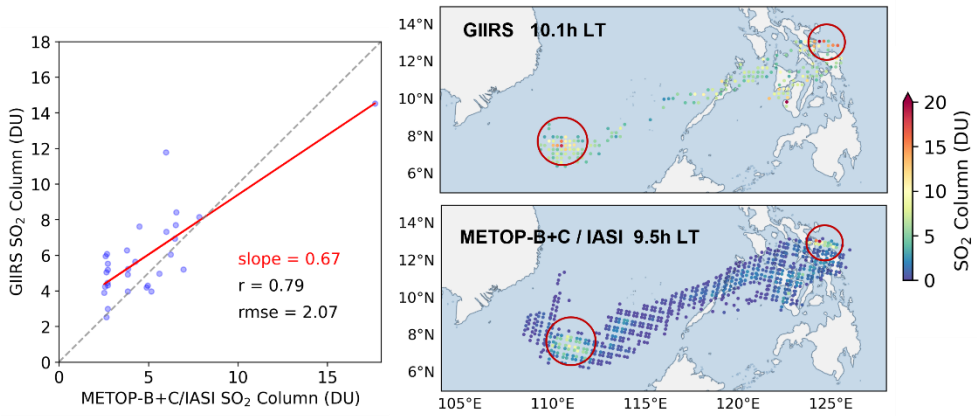

(b)

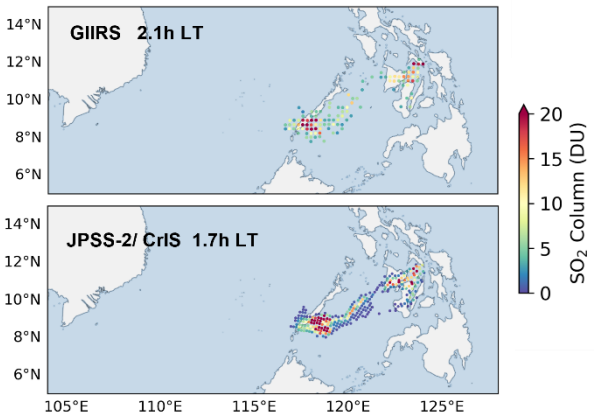

Figure S19. Visual comparison of SO_2 total columns between FY-4B/GIIRS and (a) Metop-B/C IASI, (b) JPSS-2 CrIS. Panels illustrate the consistency in plume morphology, as temporal mismatches preclude direct point-to-point quantitative validation.

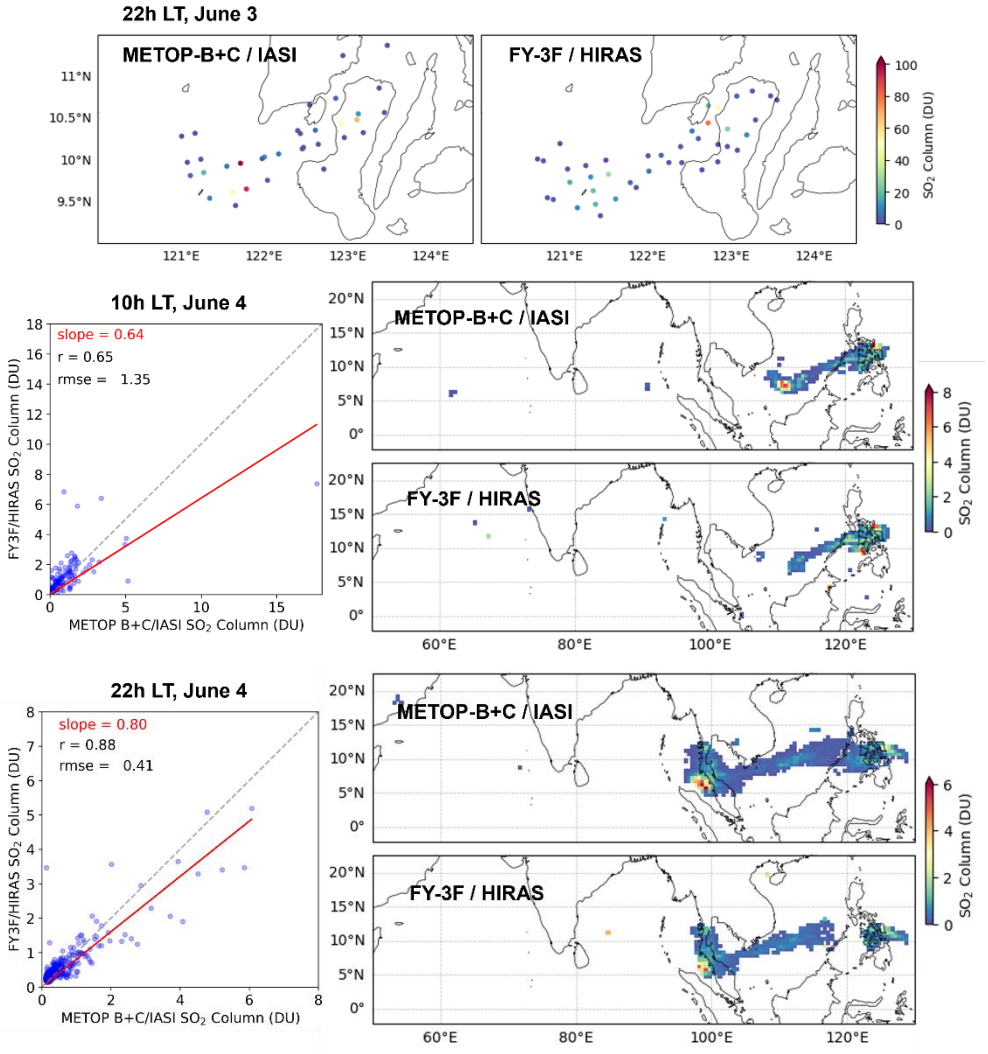

Figure S20. Similar to Fig. 9a but showing additional spatial comparisons of SO_2 total columns between Metop-B/C IASI and FY-3F/HIRAS during June 3–4, 2024.

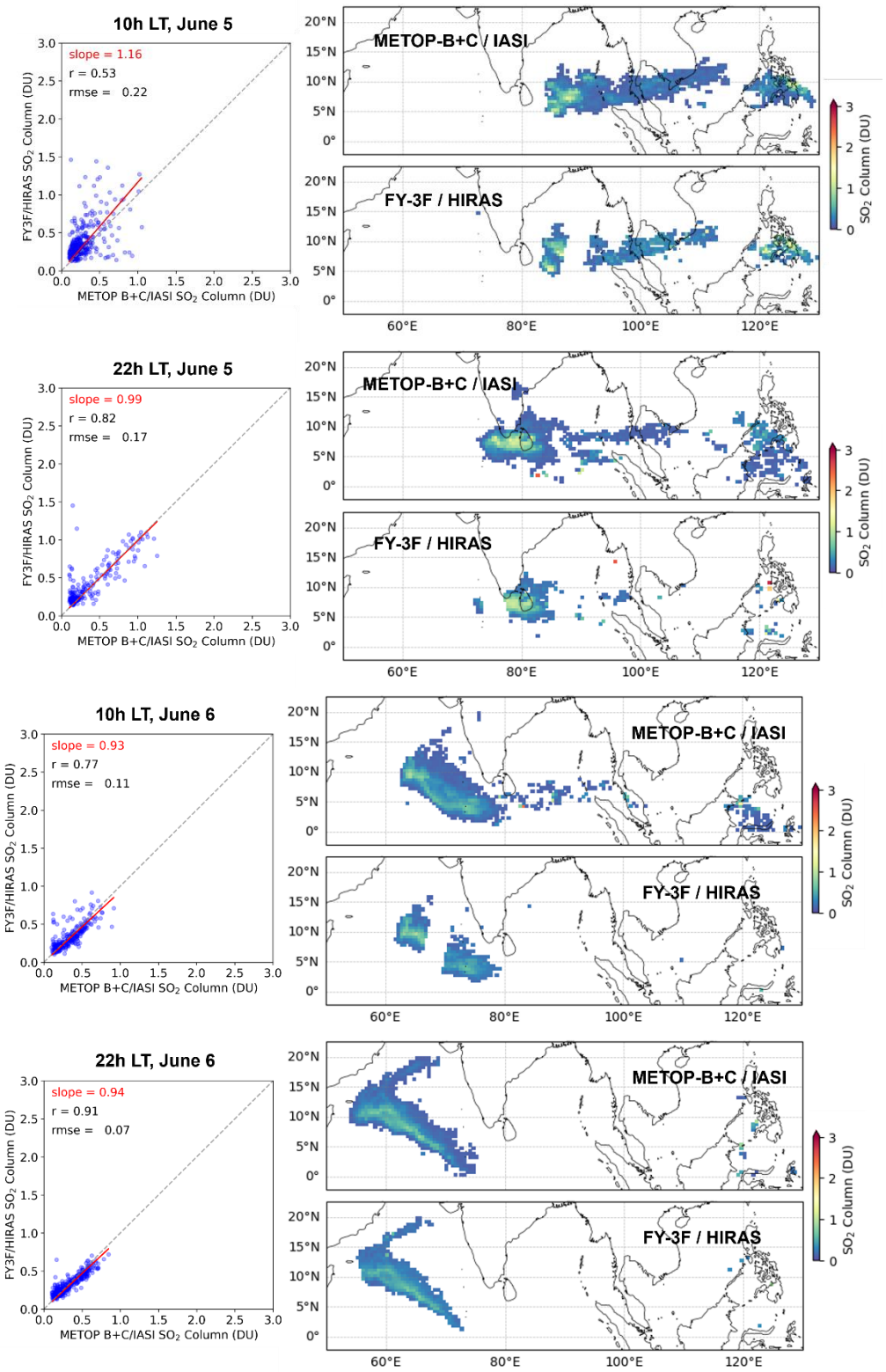

Figure S21. Same as Fig. S20, but for June 5 and 6, 2024.

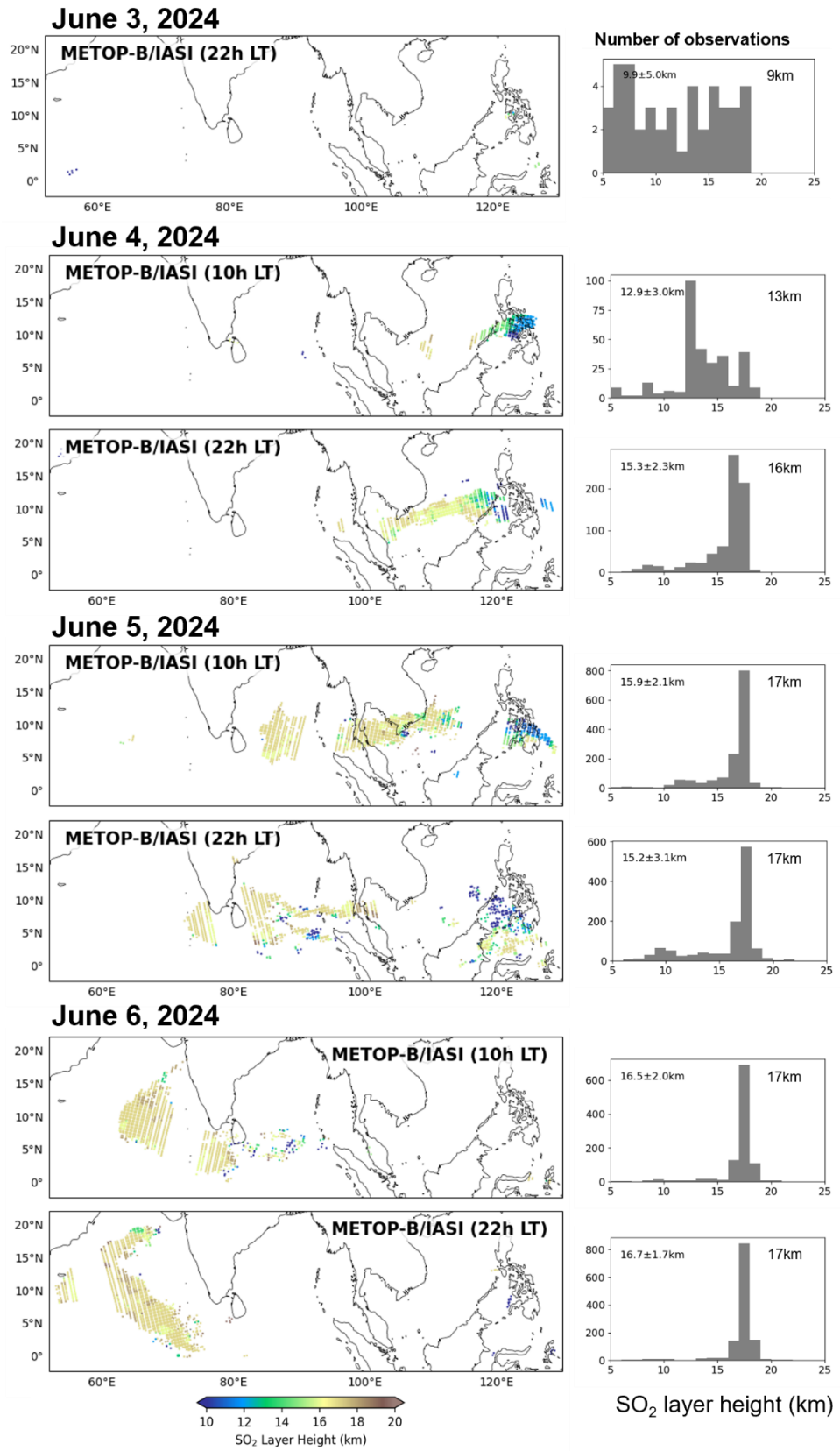

Figure S22. The spatial distribution of the IASI SO_2 plume height and the corresponding histograms for the observations on June 3–6, 2024. The inset numbers within each histogram indicate the statistical characteristics of SO_2 height: the values on the left represent the mean ± standard deviation, while the value on the right represents the median.

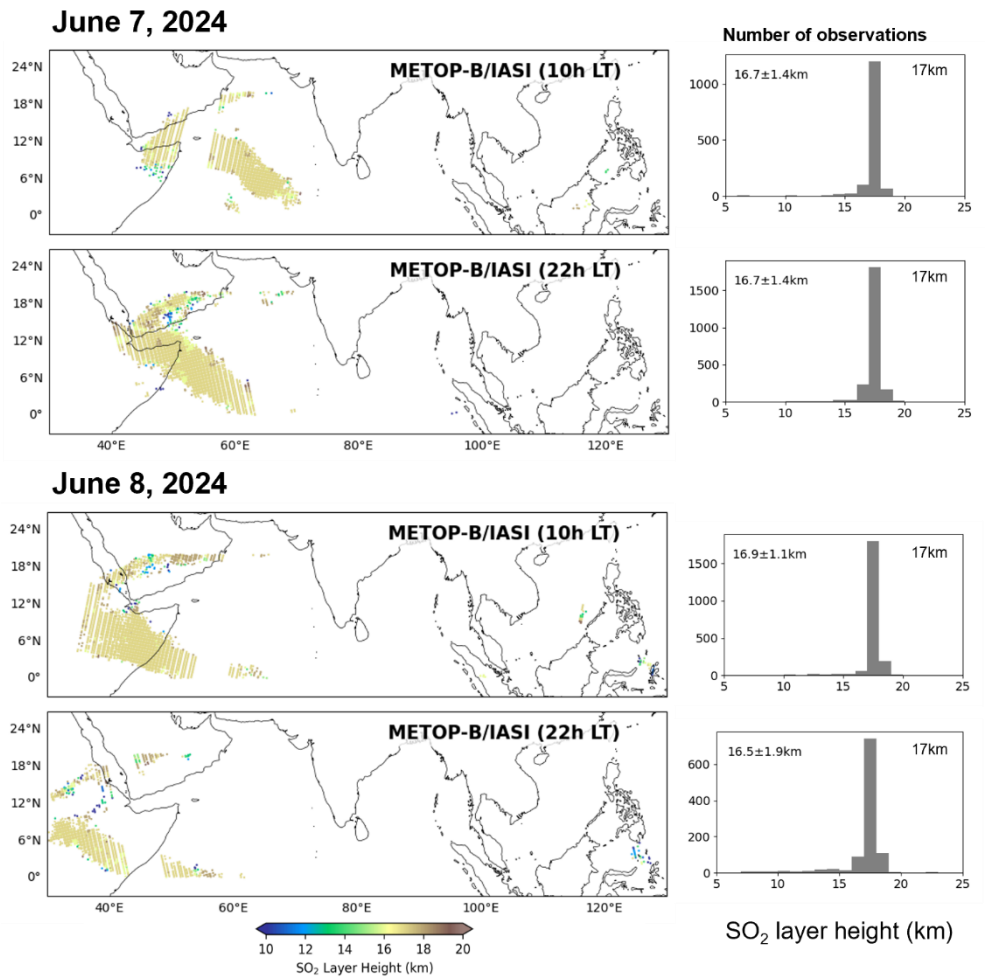

Figure S23. Same as Fig. S22, but for June 7 and 8, 2024.

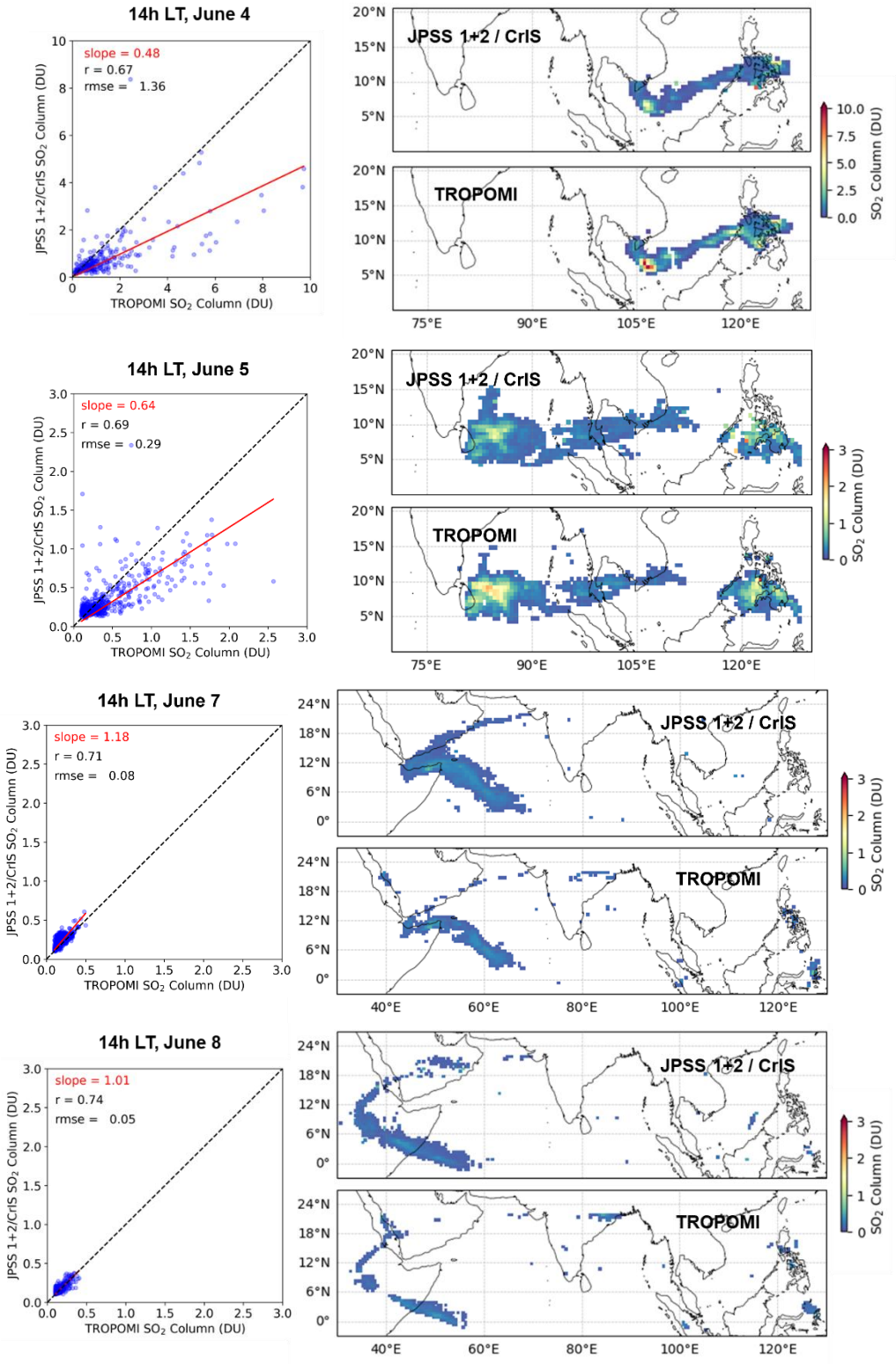

Figure S24. Similar to Fig. 10c but showing additional spatial comparisons of SO_2 total columns between JPSS-1/2 CrIS and TROPOMI during June 4–8, 2024.

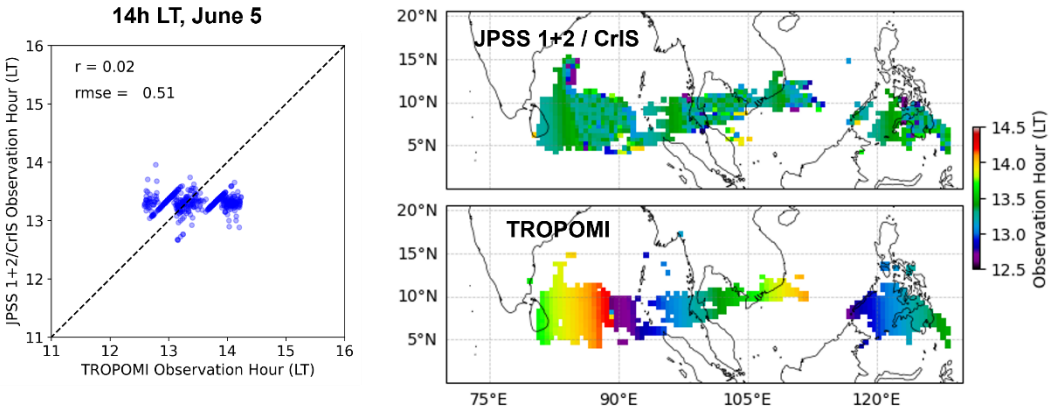

Figure S25. The mismatch of observation time between JPSS-1/2 CrIS and TROPOMI.

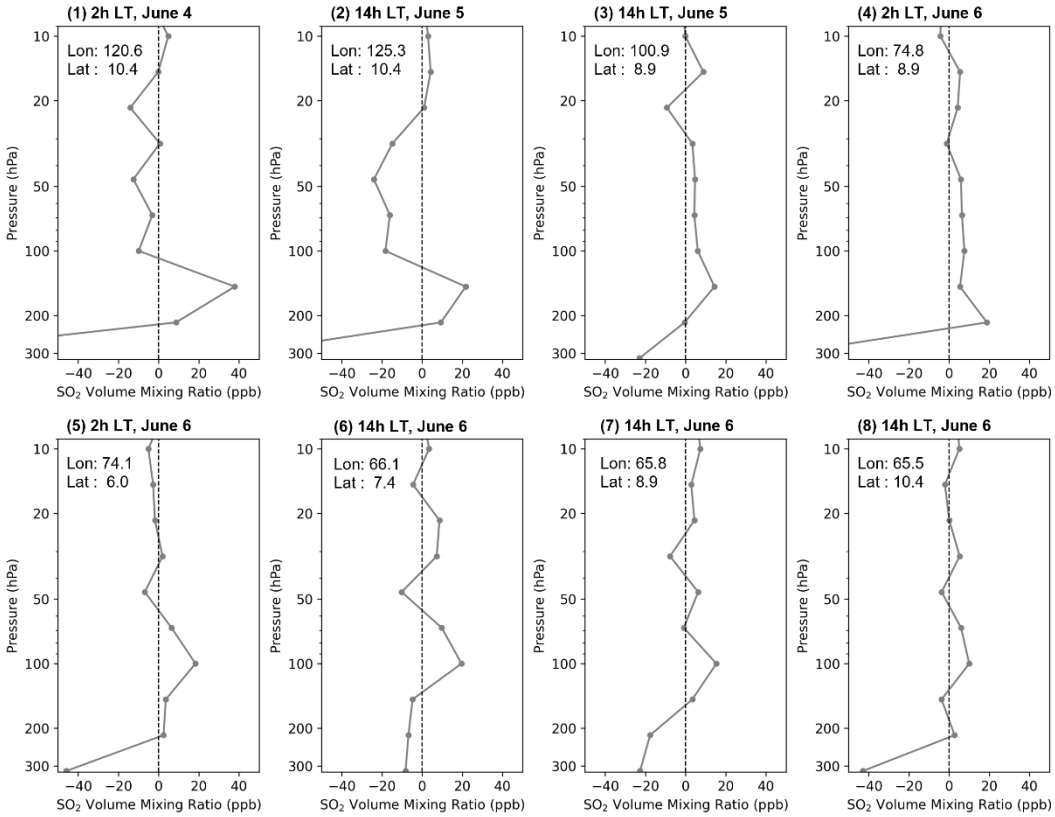

Figure S26. Aura/MLS SO_2 vertical profiles corresponding to the specific footprints marked in Figure 11. Panels (1)–(8) display the vertical distribution of Volume Mixing Ratios (VMR) against pressure for the selected geolocation points. The coordinates (latitude/longitude) and observation times are annotated in each panel.

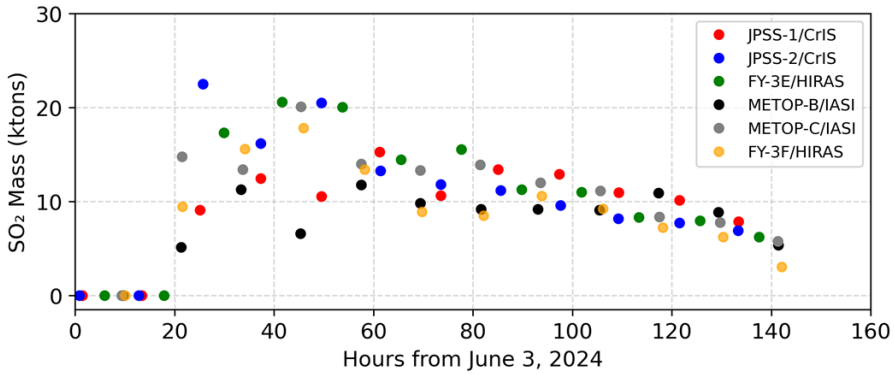

Figure S27. Time series of SO_2 mass loading derived from individual polar-orbiting infrared sensors without spatial gap-filling.

(a)

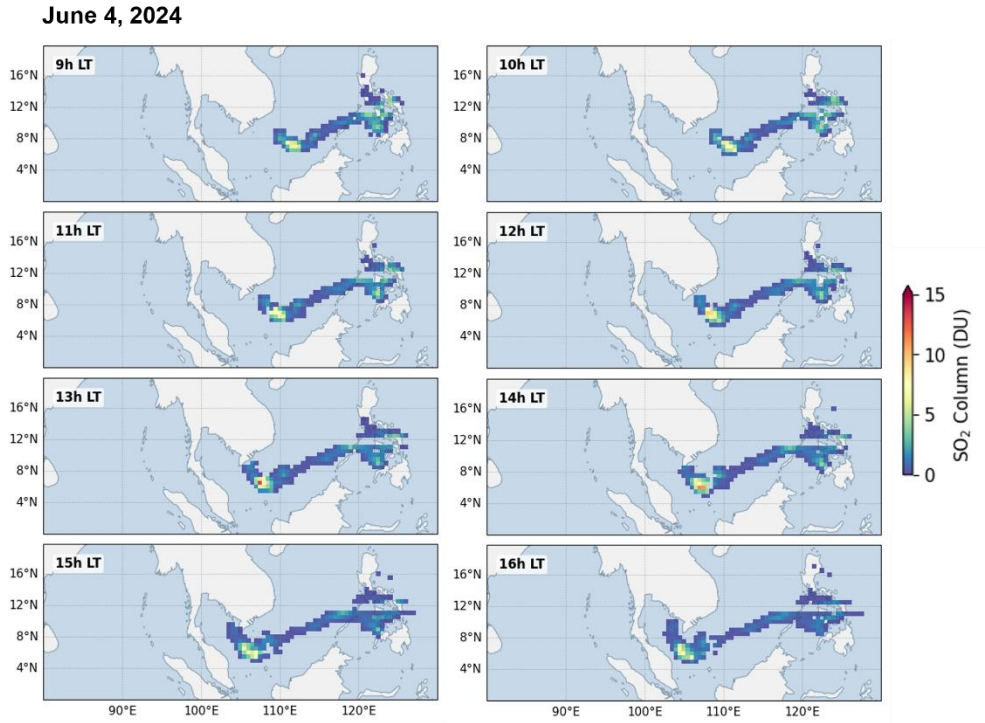

(b)

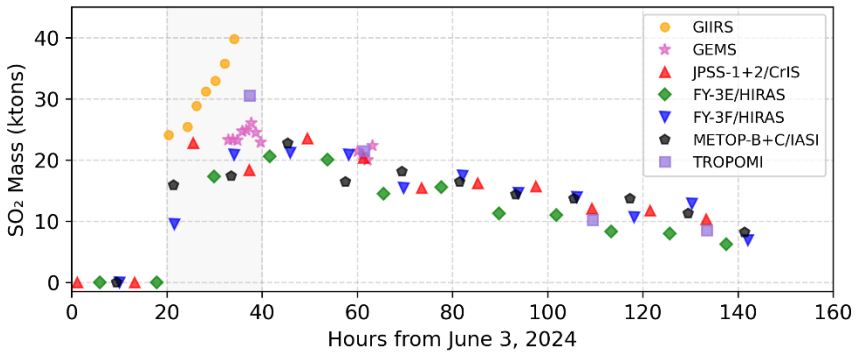

Figure S28. Impact of cloud screening on GEMS SO_2 mass quantification. (a) Similar to Fig. 7 but with a cloud fraction threshold (< 0.7) applied. The resultant spatial discontinuities within the plume indicate the rejection of SO_2-rich pixels mixed with clouds. (b) Time series of SO_2 mass loading derived from the cloud-screened dataset, revealing a systematic underestimation compared to the baseline results (Fig. 12a) due to the compromised spatial integrity.

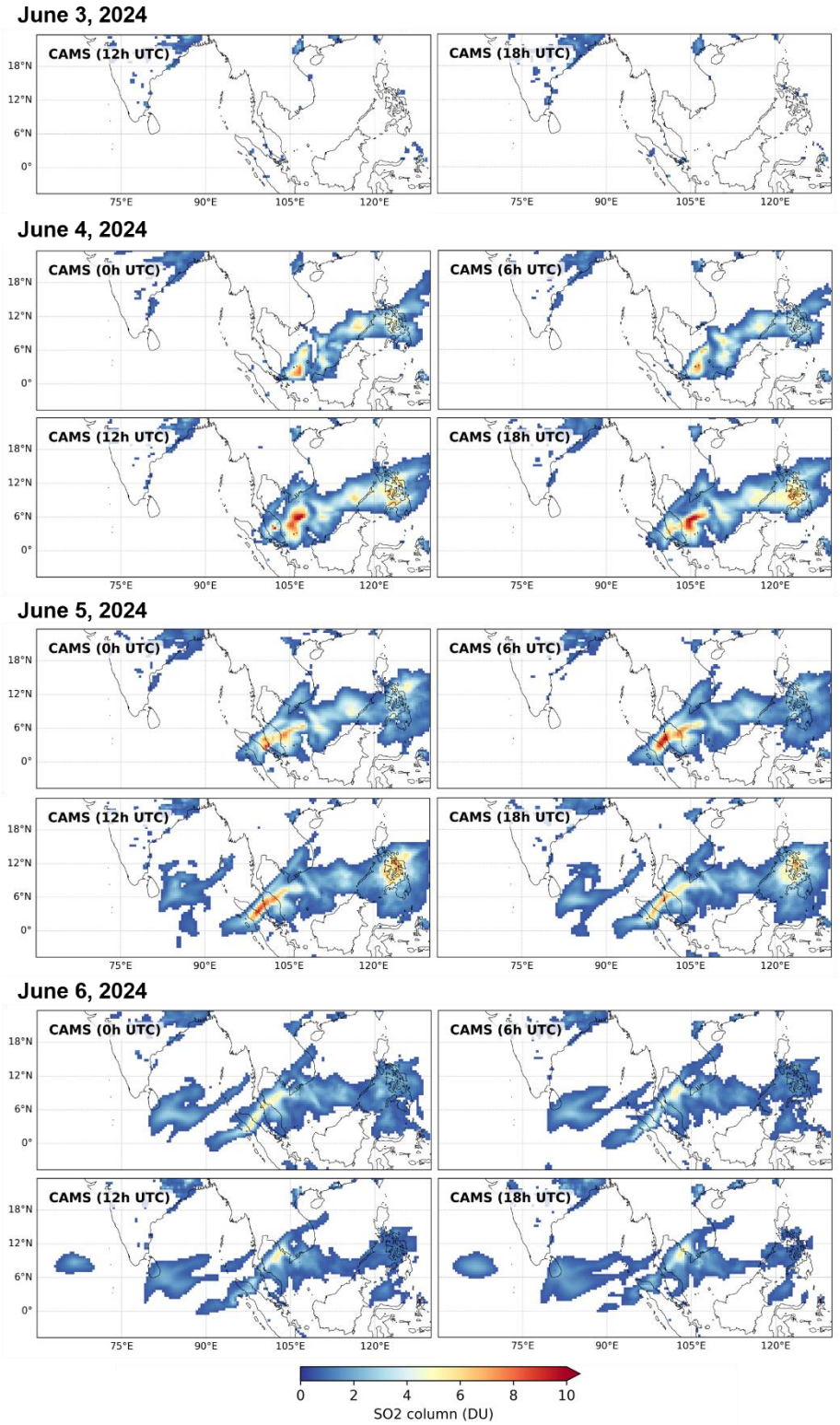

Figure S29. Spatiotemporal evolution of SO_2 total columns simulated by the CAMS forecast model. The panels display model snapshots at 6-hour intervals (00:00, 06:00, 12:00, and 18:00 UTC) from June 3 to June 6, 2024, showing the predicted transport trajectory.

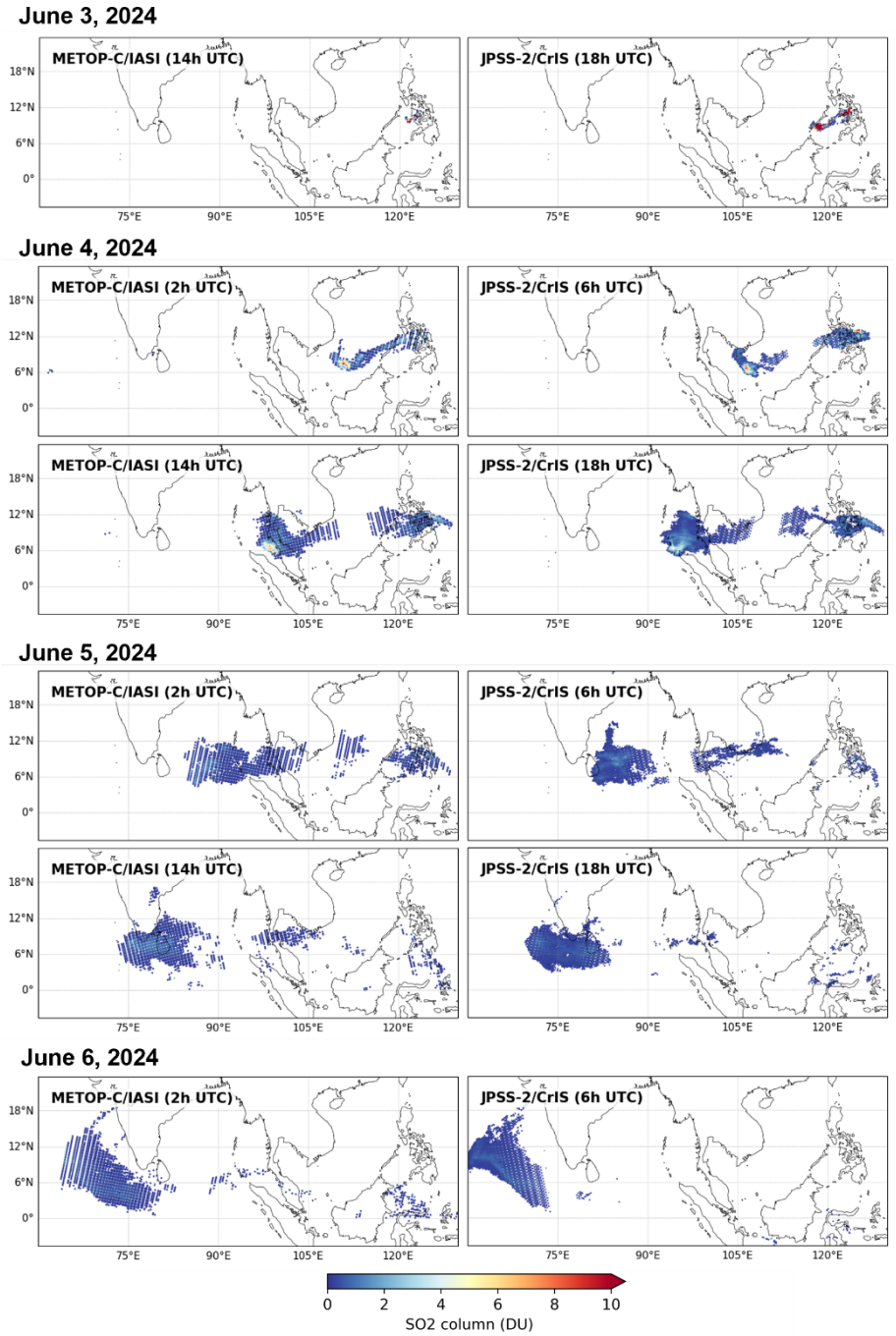

Figure S30. Satellite-observed SO_2 total columns (CrIS and IASI) temporally aligned with CAMS simulations. The observations are selected to match the CAMS output times in Fig. S29 (UTC) to facilitate direct comparison of plume morphology and transport speed.

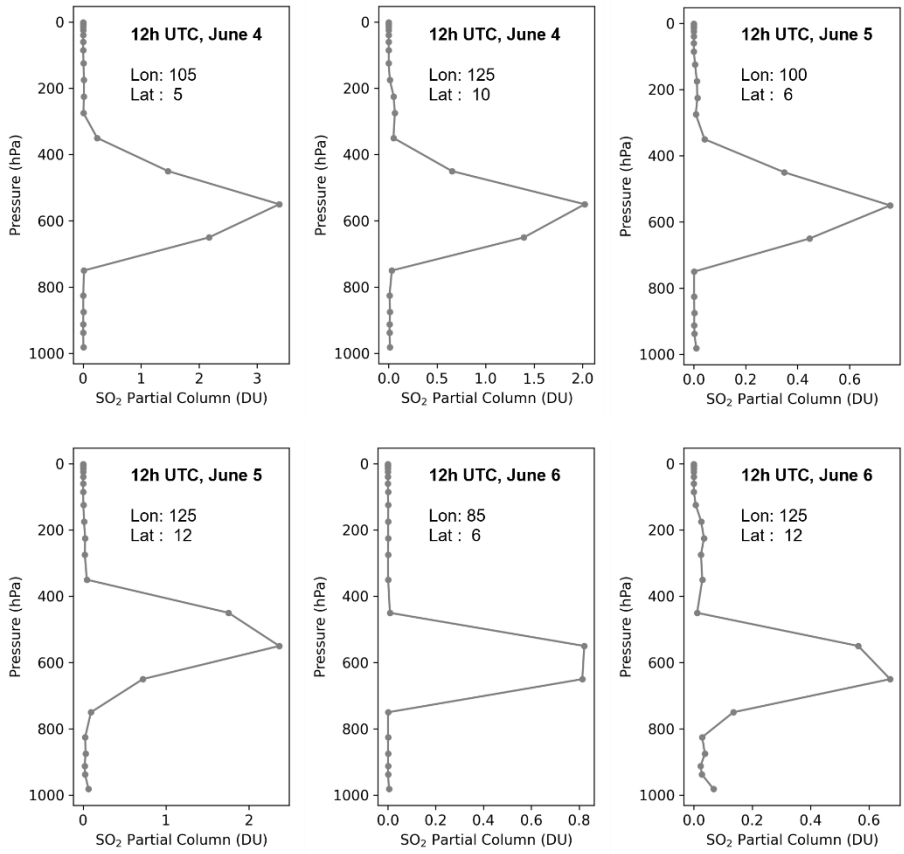

Figure S31. Vertical profiles of SO_2 simulated by the CAMS forecast model at selected spatiotemporal points. The panels display the vertical distribution of SO_2 partial columns against pressure levels for June 4–6 (12:00 UTC).